8

Mixing and Contacting of Heterogeneous Systems[*]

Asterios Gavriilidis and Panagiota Angeli

Bringing two non-miscible phases together, gas and liquid or liquid and liquid, has various applications. One group consists of reaction, separation and analysis processes and includes multiphase reactions, absorption, stripping, extraction, crystallization, nanoparticle synthesis, water oxygenation/purification, gas purification, polymerization, oil recovery and DNA analysis. In this case, efficient mass transfer is a key requirement and hence large interfacial area and mass transfer coefficients are important criteria [1, 2]. In the second group, the outcome of phase mixing/contacting is the final product and often the bubble/droplet size and its size distribution are important for ensuring high quality. These products are emulsions, suspensions, particles and encapsulated liquids with applications in pharmaceuticals (drug delivery systems), medicine (ultrasound contrasting agents, thrombus/tumor treatment), food processing (low-fat spreads), paints, inks, toners, cosmetics, perfumes and electrooptic devices [3, 4]. The formulation of such products commonly involves mixing two fluids in bulk processes [5]. This allows little control over individual units and a broad size distribution is typically produced. However, microfluidics and microchemical processing allow one to manipulate individual units precisely, control their properties and achieve better uniformity.

Depending on the ultimate objective, different approaches to contacting are available, offering distinct advantages. The type of flow obtained depends on contactor design in addition to the system properties and operating conditions. These influence the relative importance of gravitational, inertial, viscous and interfacial forces. The dimensionless numbers which provide an appreciation of the relative importance of these forces are the following:

- Bond number $\quad Bo = \Delta \rho g d^2/\gamma \quad$ (gravitational force/interfacial force)
- Reynolds number $\quad Re = \rho U d/\mu \quad$ (inertial force/viscous force)
- Capillary number $\quad Ca = \mu U/\gamma \quad$ (viscous force/interfacial force)
- Weber number $\quad We = \rho U^2 d/\gamma \quad$ (inertial force/interfacial force)

[*]A List of Symbols can be found at the end of this chapter.

In microstructured components, characteristic lengths are small and this often leads to interfacial forces dominating. Furthermore, flow confinement between microchannel walls gives rise to different behavior for various hydrodynamic phenomena. Various reviews have addressed issues pertinent to multiphase contacting and mixing [2, 4, 6–9].

There are basically two approaches for bringing in contact two phases: the first is to disperse one phase into the other by using upstream of the contactor section an appropriate inlet or a micromixer similar to those used for mixing of homogeneous systems (*dispersed-phase microcontactors*). The second is to keep both phases continuous and use the contactor to create an interface between them (*continuous-phase microcontactors*). In dispersed-phase contactors, the contactor is often a microchannel or even a larger sized tube, containing a suitable inlet to induce merging of the two phases. The inlet contains a dual feed arrangement or a multiple feed structure that splits the phases and can lead to the formation of bubbles or droplets. After the inlet section, both phases are delivered in a single contactor region. The hydrodynamics obtained depend on various parameters but the most critical are the contactor (and particularly inlet) geometry and the ratio of flow rates of the two phases. In gas–liquid systems, the *segmented* flow obtained ranges from bubbly flow – when bubbles have a smaller diameter than the contactor channel (*bubbly flow microcontactor*), to slug (or Taylor) – when bubbles have a larger equivalent diameter than the contactor channel (*slug flow microcontactor*) as the gas-to-liquid flow rate ratio increases. At very high values of this ratio, annular flow is obtained – a thin liquid annulus film surrounds a gas core (*annular flow microcontactor*) and hence the contactor becomes a continuous-phase contactor. When confined spaces are created in the main contactor channel by incorporating particles or microposts (*packed microchannel contactor*), they promote the splitting of the phases to even smaller domains, further enhancing contact area between them. Alternatively, additional confinement can be introduced to the mixing area to further increase interfacial area. In this case, a fine interdispersion of one phase into the other can be created (*foam and bubble suspension microcontactor*). Analogues of most of the above contacting approaches exist for liquid–liquid systems (e.g. droplet flow microcontactor). Even though in dispersed-phase contactors transport limitations between the two phases are significantly reduced, there is generally a degree of uncertainty concerning the actual fluid domain geometries and available interfacial areas. Coalescence of the dispersed phase is always an issue. However, the confinement offered by microstructures and the uniform bubble/droplet size distributions that can be obtained counteract this problem to a certain extent. Furthermore, if separation of the two phases at the end of the process is desired, this could be problematic as gravity, often used in large-scale operations, is negligible. Phase separation structures or devices may therefore need to be incorporated downstream of the contacting region, if the phases need to be collected separately. In continuous-phase microcontactors, the two phases form two streams which are fed separately in two suitable regions of the contactor and are (ideally) also withdrawn separately at the contactor outlet. The crucial design issue of these contactors is the way in which the interface between the two phases is stabilized. In *overlapping microchannel* and *micromesh contactors*, the interface

is stabilized by the menisci that form in small openings. In the *falling film micro-channel contactor*, gravity in conjunction with microstructured plates create and stabilize the liquid film. The advantage of such contactors is that since the phases are not intermixed the gas–liquid interfaces are well-defined. Furthermore, their use is advantageous in cases where interdispersion processes result in foams or mists which may be difficult to break in order to separate the phases. Apart from flow confinement within channel walls, modification of the wetting properties of the wall surfaces can pin the fluid–fluid interfaces and prevent flow instabilities to break them up, thus creating virtual walls within which fluid streams flow in parallel. This has been demonstrated for gas–liquid flows, where self-assembled monolayer chemistry was used in combination with either multistream laminar flow or photolithography to pattern the surfaces [10].

8.1
Gas–Liquid Systems

In two-phase microcontactors, patterns similar to those seen in large-scale flows are observed but the dominance of surface tension forces over gravity causes differences in flow pattern transitions. Three main regimes can be distinguished based on the relevant importance of the various forces. Surface tension dominated regimes with typical patterns of Taylor and bubbly flow, inertia dominated regimes with typical patterns of dispersed liquid and annular flows and intermediate regimes with typical patterns of Taylor–annular and churn flows. The stratified pattern which can still be seen in channels with diameter above 1 mm disappears as the channel dimensions diminish. A typical flow pattern map can be seen in Figure 8.1.
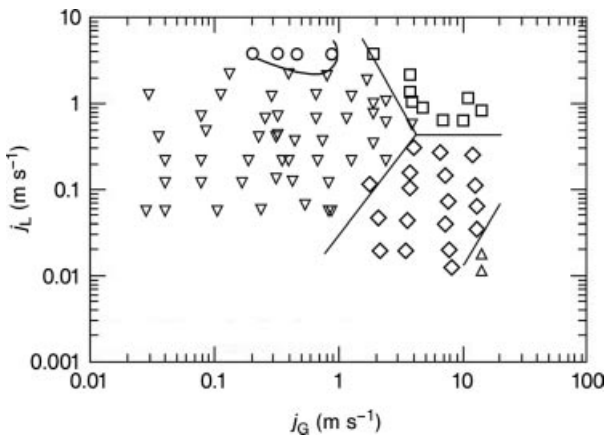

Figure 8.1 Flow patterns obtained during nitrogen–water flow in a circular channel of 530 μm diameter. ○, bubbly; ▽, slug; □, churn; ◇, slug–annular; △, annular. From [13].

Taylor and bubbly flows appear at low gas velocities and annular flows at high gas velocities (high inertia). As the channel dimension decreases, Taylor and annular flow predominate [11, 12] while patterns specific to small channels appear (such as ring, liquid lump, yakitori and rivulet flows) which can be considered as variations of the Taylor and annular flow regimes. At very small channels (with 50 and 100 μm diameter) Chung and Kawaji [13] only observed Taylor flow. Although flow patterns have mainly been investigated in circular tubes, some comparisons with non-circular channels of similar hydraulic diameter did not reveal significant differences in the flow patterns, while contradictory results in the flow pattern boundaries were obtained [11, 14]. Wall wettability has been found to affect flow pattern transition lines whereas highly wetted walls stabilize the liquid films [15]. From the few studies available on the effect of fluid properties on flow patterns, it was found that decreasing surface tension would delay the transition from Taylor to bubbly flow to higher liquid velocities and to annular flow to lower gas velocities [16, 17]. An increase in liquid viscosity has similar effects [17]. Unified flow pattern maps based on either the phase superficial velocities, phase Weber numbers or their combination with phase Reynolds numbers have been suggested with limited success [17, 18]. In square geometries, Cubaud and Ho [19] found that transitions between flow regimes occurred at the same liquid fractions in different sized channels. It is possible that different physical phenomena described by different parameters are responsible for each transition and for that reason it is not possible to describe all transitions by a unified map, where the same dimensionless parameters are used for all transitions. Moreover, the geometry of the inlet plays a significant role on the mechanism of bubble formation (see Section 8.1.1) and on the type of pattern that forms, but usually it varies widely between different investigations and that contributes further to the difficulty in standardizing the transition lines. Models for each flow pattern boundary that exist for large-scale pipes do not transfer successfully to small channels [14]. A criterion for flow pattern transition was established by Cubaud and Ho [19] for a cross-flow inlet, who argued that at liquid fractions >0.04, the higher pressure drop of the liquid compared with that of the gas results in a bubble break-up time proportional to the liquid flow rate, whereas at lower liquid fractions the gas pressure drop can sustain that generated by the liquid and the flow becomes annular.

8.1.1
Segmented Flow Contactors

In Taylor flow (also referred to in the literature as bubble train, slug, segmented, plug, elongated bubble or intermittent flow), the gas bubbles are separated by liquid slugs (Figure 8.2). The presence of bubbles in front of and at the back of the slugs modifies the flow field in the liquid compared with single-phase flows and toroidal vortices along the length of the slug can form. The recirculation within the liquid slugs improves heat and mass transfer from liquid to wall and interfacial mass transfer from gas to liquid [20, 21]. In addition, the separation of the bulk liquid by the bubbles significantly reduces axial mixing in the liquid as the very thin film surrounding the bubbles is the only means of communication between two successive slugs [22]. Microcontactors operating under
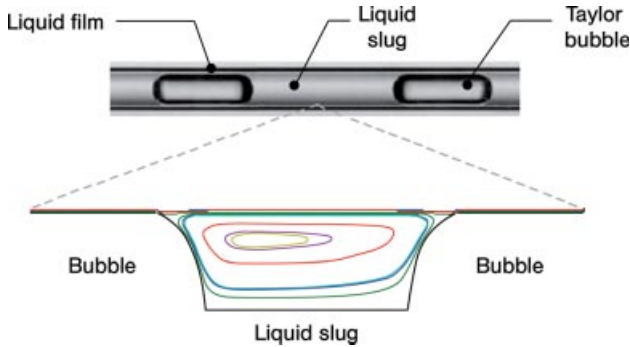
Figure 8.2 Taylor flow in a capillary and flow streamlines within the liquid slug.

Taylor flow have many similarities with monolith reactors. A lot of work on Taylor microchannel flow has been aimed at understanding and improving the conditions within monolithic reactor channels [23]. Because of its low axial mixing properties, Taylor flow can be used in high-throughput screening [4]. Even microfiltration efficiencies have been found to improve in the Taylor flow regime [24].

8.1.1.1 Bubble Formation and Length

For systems of T- inlet design, where all channels connecting to the inlet junction have similar diameters, at low capillary numbers ($Ca < 10^{-2}$) interfacial forces dominate shear stresses and the dynamics of break-up are dominated by the pressure drop across the emerging bubble/droplet [25]. The shear stresses exerted on the interface of the emerging bubble are not sufficient to distort it significantly and the bubble blocks almost the entire cross-section of the main channel, confining the flow of the carrier fluid to the wetting films adjacent to the microchannel walls. This increases the pressure upstream of the emerging bubble and leads to the squeezing of the neck connecting the forming bubble with the gas inlet. In this *squeezing* regime, the process of break- up is independent of Ca and thus of viscosity and interfacial tension. The length of the bubble can be obtained by

$$\frac{L_s}{w} = 1 + \frac{aQ_d}{Q_c} \tag{8.1}$$

For $a = 1$ this equation also predicts Taylor bubble length obtained in mixing sections of cross geometry with square channels [26] and in co-flow geometry [27]; in the latter case, when bubbles with irregular shapes are formed, the equation can still predict the equivalent bubble length. At low gas flow rates, the bubble volume remains essentially constant and the frequency of bubble production is proportional to gas flow rate (*constant volume* formation regime). For larger gas flow rates, bubble frequency levels off and bubble volume increases in proportion to the gas flow rate (*constant frequency* formation regime) [26].

Bubble (and slug) lengths have been obtained experimentally or through computational fluid dynamic simulations [28–30]. These revealed that sizes are mainly affected by gas and liquid superficial velocities and contactor size and slightly by

surface tension, whereas the results on the effect of viscosity were contradictory. The different inlet geometries used perhaps contributed to the discrepancies between the empirical correlations. To demonstrate the effect of inlet design on the size of the bubbles formed, Qian and Lawal [31] carried out simulations using different degrees of premixing for the two fluids and found that small mixing zones favored short bubbles and slugs.

In T- and Y-junctions with different inlet channel dimensions and fluid joining angles and in a co-flow configuration, Amador *et al.* identified three main bubble formation mechanisms [32]. One of them, which involves bubble lift-off, neck formation between the bubble and the gas inlet and finally neck break-up and bubble detachment, resembles the mechanism of bubble formation from an orifice in an infinite liquid medium. Bubble pairing was also observed at the inlet and, when small non-Taylor bubbles formed, there was bubble coalescence in the main channel. Bubble length was found to depend mainly on the ratio of gas to liquid superficial velocities. The size of the gas inlet affected bubble size but not that of the liquid inlet. Furthermore, the angle between the two fluid inlets had a small effect on bubble size. In a co-flow configuration, Xiong *et al.* [27] observed a two-step mechanism: gas ligament expansion, where the bubble neck forms, and gas ligament collapse, where the neck breaks and the bubble detaches. Increasing viscosity reduced bubble size, while decreasing surface tension resulted in bubbles with irregular shapes.

8.1.1.2 Hydrodynamics

The presence of bubbles affects the flow field within the liquid slugs and results in fluid recirculation [33]. At low Ca, there is a stagnation ring at each bubble cap (Figure 8.2). For $0.6 < Ca < 0.7$ there is still recirculation in the liquid accompanied by two stagnation points: on the bubble front and inside the liquid. At $Ca > 0.7$, complete bypass of the liquid occurs with a single stagnation point at the bubble front [34, 35]. Thulasidas *et al.* [34] found theoretically that complete bypass occurs at $Ca > 0.5$ in upward flow and at $Ca > 0.6$ in downward flow. In square channels, liquid bypass was found to occur at $Ca > 0.54$ for horizontal flow [36], whereas in upward and downward flows complete bypass occurred at $Ca > 0.5$ and $Ca > 0.57$, respectively [34].

8.1.1.3 Bubble Shape and Film Thickness

The film that surrounds the Taylor bubbles affects mass transfer and is related to bubble velocity and gas holdup in the channel. Initial experimental findings that the film thickness was proportional to $Ca^{1/2}$ were confirmed and extended to $Ca = 10^{-1}$ by Taylor [33]. In his pioneering approach, Bretherton [37] used lubrication theory and found that the film thickness is given by $\delta/d_{\mathrm{t}} = 0.66 Ca^{2/3}$. Although this finding should be valid for low Ca, experiments agreed better with the theory for $Ca > 10^{-3}$, whereas at lower Ca, where the theory should hold exactly, the film thickness was substantially larger than the theoretical values. This discrepancy was later attributed to the presence of surface-active contaminants absorbed at the interface. Ratulowski and Chang [38] demonstrated that surface contamination could be correctly assessed if surface tension is allowed to vary along the interface and surfactant transport in the

bulk is mass transfer limited. For higher values of Ca ($Ca > 5 \times 10^{-3}$), numerical studies are required to obtain bubble shape and film thickness. Based on scaling arguments in a semi-infinite bubble, Aussilous and Quéré [39] suggested a correlation for film thickness in the viscocapillary regime (where the film thickness depends only on Ca) that agreed well with Taylor's data and at very small Ca with Bretherton's model. After fitting it against experimental data the correlation became

$$\frac{\delta}{d_t} = \frac{0.66 Ca^{2/3}}{1 + 2.5(1.34 Ca^{2/3})} \tag{8.2}$$

At $Ca > 10^{-3}$, inertial effects become important (visco-inertial regime) and the film thickens as suggested by Taylor's data. In this regime

$$\frac{\delta}{d_t} \propto \frac{Ca^{2/3}}{1 + Ca^{2/3} - We} \tag{8.3}$$

Computationally it was found that the influence of increasing Re on film thickness is non-monotonic where an initial decrease in thickness is followed by an increase [40]. For $Ca < 0.01$, however, inertial forces do not have an effect on film thickness. Experimentally determined film thickness correlations were listed by Edvinsson and Irandoust [41]. Thulasidas *et al.* [34] found experimentally in 2 mm channels that the film thickness was almost the same in horizontal and downward flows but twice as much in upward flow.

Analytical and numerical investigations provided information on bubble shape [35, 37, 40, 41]. The bubble front tends to adopt the shape of an arc of a circle for decreasing Ca. Undulations appear at the back of the bubble which depend on both Ca and Re. Larger Re values appear to produce larger undulations whereas for $Ca > 0.5$ no undulations are observed. As Ca increases, the rear of the meniscus changes from convex to flat and then to concave. For $Ca < 10^{-3}$, close to the meniscus tip the interface is an almost perfect hemisphere. The film acquires a constant thickness downstream of the bubble front and this transition region diminishes with decreasing Ca.

In square channels at $Ca < 0.1$, the bubble is not axisymmetric and flattens out against the tube walls leaving liquid regions in the corners joined by thin flat films at the channel sides. At increased Ca the bubble becomes axisymmetric and for high Ca the bubble radius reaches an asymptotic minimum value, approximately equal to 0.68 of the square channel half-width [36]. The liquid flows mainly in the corners and is very thin film at the side walls, where dry patches can appear when the wall is not fully wetted. Cubaud and Ho [19] argued that when $U_b < U_{dew}$, where U_b is the bubble velocity and U_{dew} is a dewetting velocity, the bubbles completely dry out the solid surface in the center of the channel wall, whereas when $U_b > U_C$, where U_C is the bubble velocity in the center of the channel wall at the bubble rear to dry out, the bubbles are lubricated by a thin liquid film.

8.1.1.4 Pressure Drop

For low Re, Kreutzer *et al.* [42] found that the presence of bubbles in Taylor flow increases the single-phase liquid pressure drop by an amount almost equal to the

difference in interfacial pressure between the tips of the bubble. At higher Re, however, the dramatic increase in pressure over the bubble is not represented in the overall pressure drop. Assuming that the overall pressure drop in a unit cell, that comprises a bubble and a slug, should be equal to the pressure drop in the slug plus a term that accounts for the effects of the presence of the bubble, the following correlation was suggested:

$$f = \frac{16}{Re}\left[1 + \alpha_1 \frac{d_t}{L_S}\left(\frac{Re}{Ca}\right)^{1/3}\right] \tag{8.4}$$

where α_1 was numerically found to be equal to 0.07, but experimental data were fitted better by a value of 0.17, perhaps because of the presence of impurities. At very low Ca, the equation agreed with Bretherton's [37] analytical solution. Pressure drop over the whole channel is then equal to

$$\frac{\Delta P}{L} = \frac{2f\,U_m^2 \rho_l}{d_t}\varepsilon_l \tag{8.5}$$

An empirical correlation for pressure drop has been suggested by Liu *et al.* [29]. Based on experimental data, Cubaud and Ho [19] suggested two correlations for pressure drop for gas–liquid flows depending on the liquid hold up ε_l:

- at high ε_l (bubble and elongate bubble flows): $\Delta P_{2\text{-phase}} = \Delta P_L \varepsilon_l^{-1}$
- at low ε_l (slug, annular and dry flows): $\Delta P_{2\text{-phase}} = \Delta P_L \varepsilon_l^{-1/2}$, reflecting the large slip between the two phases

where $\Delta P_{2\text{-phase}}$ and ΔP_L are the two-phase and single-phase liquid pressure drop, respectively.

8.1.1.5 Mixing and Mass Transfer

The presence of bubbles in Taylor flow reduces axial mixing and results in narrow residence time distributions [43]. At low Peclet number ($Pe = U_b d/D$), where the mixing within the liquid slugs is good, tank-in-series models can be used to predict the degree of dispersion [44]. However, at very low Pe, forward diffusion may also occur. For higher Pe, more sophisticated models have been developed where the region of the slug is divided into a closed vortex region and an enclosing open thin liquid annulus film (*two-region models*) [22, 45, 46]. Various assumptions were used for the mixedness of the two regions whereas the mass transfer between the two regions was obtained either by using mass transfer coefficients or assuming that only diffusion is taking place. Salman *et al.* [47] obtained residence time distributions using computational fluid dynamics (CFD) modeling and showed that an increase in Pe, Ca or the slug length results in larger tracer spreading in terms of time [48]. It was demonstrated that when short slugs are used, the tracer spreads to a larger number of slugs but its spread over time is lower.

For predicting mass transfer in Taylor flow, gas–liquid and liquid-wall mass transfer coefficients are required. Mass transfer coefficients from gas to liquid were found experimentally to be in the range 0.1–$0.8\,\text{s}^{-1}$ and correlations have been

suggested for their calculation [21, 49, 50]. Berčič and Pintar [21] found that the liquid slug length influenced the gas–liquid and liquid–wall mass transfer coefficients much more than bubble length. In order to model the gas to liquid mass transfer, two different contributions to the overall mass transfer coefficient are considered, from the cylindrical part of the bubble and from the bubble ends. Liquid to wall mass transfer coefficients have also been obtained through experiments and CFD simulations and a correlation has been proposed [51]. Shorter slugs were found to yield higher values of the mass transfer coefficient whereas the film–wall mass transfer was found to be worse than the slug–wall mass transfer. Using a simplified model, where the liquid film around the bubbles is ignored, Kreutzer *et al.* [23] demonstrated that mass transfer from liquid to wall could be an order of magnitude faster that in single-phase flow through a capillary.

Recently, meandering channels were used to improve radial mixing further in Taylor flow. Using micro-particle image velocimetry (PIV), Günther *et al.* [43] observed that mixing is accelerated by the periodic switching of the recirculation patterns within the liquid slugs and is more efficient than in homogeneous chaotic mixers (Figure 8.3). In addition, surface roughness and compressibility of the gas phase further improved radial mixing. Interfacial areas in Taylor flow have been measured and related to the Weber number [52]. The maximum interfacial areas of $19\,000\,\mathrm{m^2\,m^{-3}}$ for 2-propanol–nitrogen and of $18\,000\,\mathrm{m^2\,m^{-3}}$ for water–nitrogen systems were observed at similar Weber numbers above 1.5.

8.1.1.6 Phase Separation

The separation of phases at the segmented flow channel outlet can be problematic and a number of approaches have been suggested that aid separation and reduce pressure fluctuations as the bubbles exit. Hsieh and Yao used a separator consisting of two parallel silicon wafers each containing an array of etched through holes [53]. One wafer was made hydrophilic to facilitate liquid removal and the other hydrophobic to prevent the liquid leaking through it. Günther *et al.* separated liquid from gas in a separator that consisted of 16 capillaries, each $20\,\mu\mathrm{m}$ wide, that is wetted by the liquid [43]. Liquid was withdrawn by applying a pressure difference smaller than the capillary pressure across the microchannel so that only gas remained in the main channel.
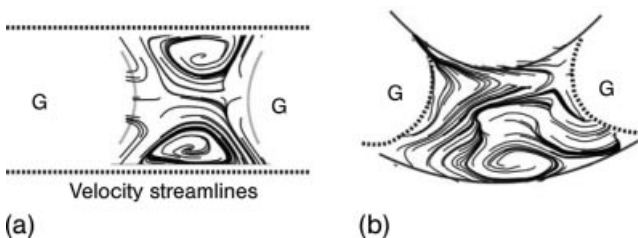
Figure 8.3 Flow streamlines in a liquid slug during Taylor flow in (a) a straight channel and (b) a meandering channel. From [43].

8.1.1.7 **Multichannel Systems**

A scaled-out version of a single-channel Taylor-flow reactor, which was called a microbubble column, was presented by Hessel *et al.* [54]. In this device, the gas and liquid feeds were split into a number of substreams and were subsequently brought into contact in the reaction channels so that one gas and one liquid substream were introduced into one reaction channel. To achieve flow equipartition, the gas- and liquid-inlet channels were designed with different hydraulic diameters (7 and 20 μm, respectively). The reaction channels were 50×50 μm or 300×100 μm in cross-section. Various flow patterns were found in the different channels [52]. A two-channel dispersed phase microreactor was designed by de Mas *et al.* [55]. A single inlet was used for the liquid and there were two gas ports. At the outlet, the two reaction channels merged and the fluids exited via a single port. The reaction channels had a triangular cross-section and a number of patterns were obtained (bubble, annular, slug–annular, churn) with dry patches appearing during annular flow.

8.1.2
Packed Microchannel Contactors

Mixing gas and liquid phases can benefit from the presence of a high solid interfacial area over which thin fluid streams can be generated and maintained. This can be accomplished by placing microcolumns inside a microchannel to form a micro-machined packed-bed contactor [56]. Introducing surface forces in the center of the channel provides an added level of control over the two-phase flow and flow transitions. The fluid streams are brought into contact by a series of interleaved inlet channels. A fixed bed can also be formed by immobilizing solid particles inside an empty microchannel with the aid of a microfilter [57]. However, the microstructured version avoids the randomness in packing that is inherent in small particle beds, which can result in high pressure drops and flow maldistribution in multi-channel systems. For the packed bed contactor with a regular array of microcolumns shown in Figure 8.4, in addition to slug and annular flow, other flow patterns are observed. Dispersed flow (Figure 8.5) is encountered when both gas and liquid flow rates are increased and is characterized by an intimate dispersion similar to
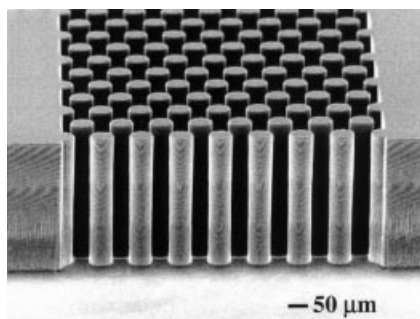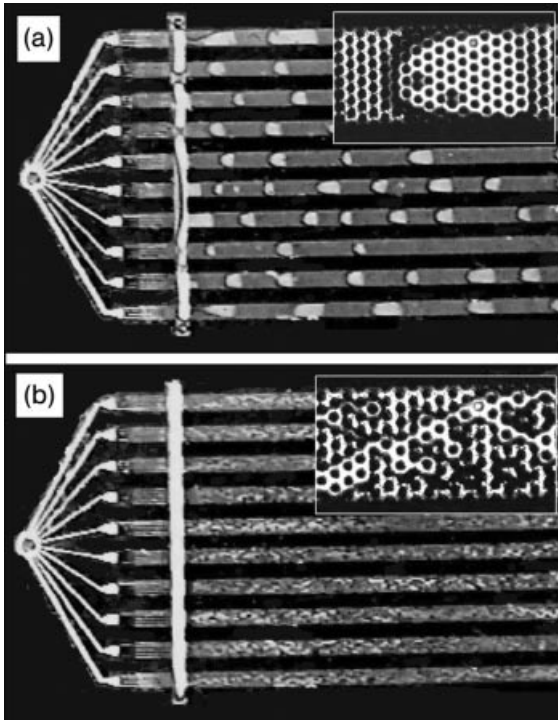

— 50 μm

Figure 8.4 Packed microchannel contactor with microfabricated columns. From [56].

Figure 8.5 Flow regimes observed for gas–liquid flow in the device pictured in Figure 8.4. (a) At low gas flow rates, the phases are segregated, as seen with the gas slug in the center of the channel (inset). (b) At high gas flow rates, the two phases are randomly dispersed throughout the microstructured channel. From [56].

bubbly flow. In this regime, mixing of the gas and liquid phases is the greatest and the interfacial area is substantially larger than in an open channel arrangement. In the dispersed flow regime an interfacial area of $16\,000\,m^2\,m^{-3}$ and for slug flow $1500\,m^2\,m^{-3}$ were estimated. In conventional trickle beds, the specific interfacial area can reach (for pulse flow) up to $500\,m^2\,m^{-3}$ [58]. In the microchannel (particle) packed bed reactor reported by Losey *et al.* [57], pulsing flow was observed, similarly to macroscale analogues, but at slightly different flow conditions. The penalty for the high surface area attained in these contactors is large pressure drop ($\sim$0.5 atm). For packed microchannel contactors with microcolumns or similar sized particles, the mass transfer coefficient was in the range 3–$15\,s^{-1}$ [56, 57, 59], an order of magnitude higher than for identical empty microchannels [60]. The increased mass transfer for the former can be attributed to the larger interfacial area created by the presence of the columns, analogous to the use of inert packing material in conventional macroscopic gas–liquid contactors. The two phases are forced to mix over the particles in a constrained volume relative to the large pellet-size in trickle-bed reactors. Typical mass transfer coefficient values for laboratory trickle bed reactor systems are

0.01–0.08 s^{-1} [61]. If one considers the penalty in terms of increased resistance to flow and hence the associated energy dissipation, the microcontactor operates as efficiently as a standard reactor [57].

8.1.3
Foam and Bubble Suspension Microcontactors

Foams are dispersions of bubbles where neighboring bubbles touch each other and form a jammed solid-like closed packing [62]. They are characterized by polyhedral bubbles and a high gas-phase fraction. When the gas fraction is relatively low, the bubbles retain their spherical shape (unless they are severely confined) and bubble suspensions are obtained. Monodisperse foams are advantageous, since coalescence, driven by the difference of Laplace pressure between neighboring bubbles, is reduced. Due to the high interfacial tension between gases and liquids, surfactants are usually introduced in the liquid phase to facilitate bubble formation and reduce coalescence.

8.1.3.1 T-type Mixing Section Geometries

A simple way to produce foams in a microchannel environment is to use a T, Y or cross geometry mixing section where the gas and liquid merge, feeding to a larger width channel. In general, for $Ca < 10^{-2}$ Taylor bubbles form according to the pressure-dominated *squeezing mechanism* described earlier. When these bubbles enter the main channel, a bubble suspension is produced as shown in Figure 8.6. Air bubble sizes of ~100 μm at low formation frequencies and larger bubbles at frequencies >1 kHz were observed for water solutions [26]. Bubble size can be
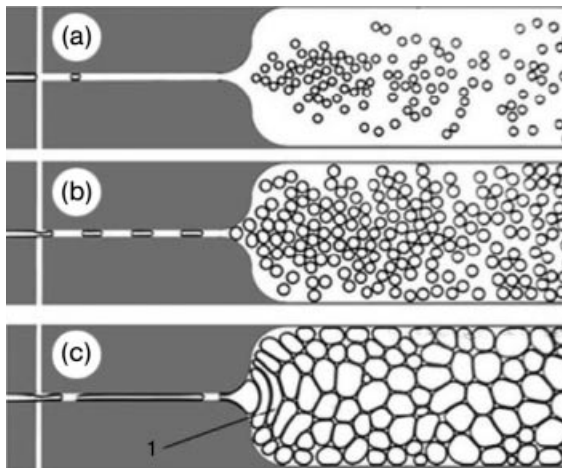
Figure 8.6 Aqueous foam flow generated with a cross geometry mixing section consisting of 100 μm square channels. Liquid fraction: (a) 0.91, (b) 0.57, (c) 0.09. From [26].

reduced by reducing the size of the channels in the mixing region. Unless shear forces are enhanced, the smallest bubble diameter that can be obtained is similar to the outlet microchannel characteristic dimension. Shear forces were increased in a microbubble beam generator which consisted of micropipette tips submerged at a right-angle to the main liquid-flow channel [63]. Since micropipettes with a hole size of 0.4–5 μm are commercially available, such a device can be constructed easily without resorting to microfabrication. Bubble size decreased to 5 μm with decreasing pipette hole size, increasing liquid velocity or viscosity, decreasing gas supply pressure and increasing liquid–pipette contact angle. One of the limitations of very small gas inlet size is that the minimum gas supply pressure for gas breakthrough to the liquid phase, leading to bubble generation, can become prohibitively high, particularly for wetting liquids.

8.1.3.2 Flow Focusing Mixing Section Geometries

With the above mixing section geometries, bubbles smaller than the characteristic width of the gas inlet channel cannot be obtained. Flow focusing (FF) devices circumvent this limitation. One type of axisymmetric FF device consists of a gas feeding nozzle positioned upstream of an orifice (50–200 μm) through which a liquid stream is forced [64]. At the mouth of the nozzle a cusp-like bubble attaches, from whose apex a steady gas ligament forms and is focused through the orifice by the surrounding liquid stream. The absolute instability of the gas ligament, which is ensured as long as Ca is below a critical value [65], provokes tip streaming of uniform bubbles, at constant frequency (Figure 8.7). If the liquid jet utilized to focus the gas is expelled into air, it eventually breaks up into uniform hollow droplets, whose density can be adjusted by the Q_g/Q_l ratio. Through this procedure, air bubbles as small as 10 μm and always smaller than the orifice ($d_b/d_{or} \approx 0.1–0.6$), were obtained. The gas fraction of the resulting suspension was typically smaller than 20%. Ganan-Calvo suggested that a radial pressure gradient developing in the liquid is important in bubble formation, because it leads to liquid acceleration which leaves room for the expanding bubble [66]. The following expression, suitable for high Re, was developed to calculate bubble diameter:

$$\frac{d_b}{d_{or}} = a \left(\frac{Q_g}{Q_l} \right)^{0.4} \tag{8.6}$$

A planar format rectangular chamber with height 30–50 μm and one small exit orifice (200–600 μm width) (Figure 8.8) can still create a gas ligament from whose tip bubbles break away, without the need for a nozzle to feed the gas [67]. Liquid feeding orifices have to be located on both sides of the exit orifice, while the gas feeding orifice is placed midway between them and located opposite the exit orifice. Such a device was used to create bubble suspensions with gas fraction up to 85% and air bubble diameters in the range 10–100 μm in water mixtures.

A two-dimensional microfabricated flow focusing geometry, containing a central channel for gas delivery, two flanking channels for liquid delivery and a focusing orifice is shown in Figure 8.9 [68, 69]. The typical height of the channels was 30 μm

(a)   (b)

(c)
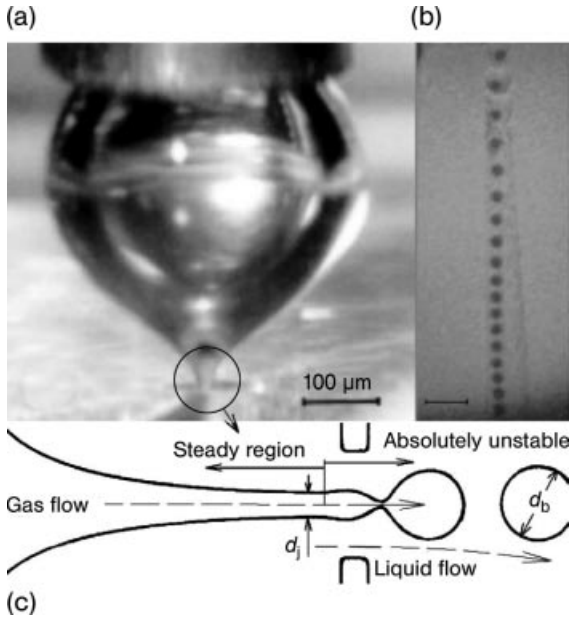
Figure 8.7 Axisymmetric flow focusing bubble generation device. (a) Cusp-like bubble attached to the capillary gas-feeding tube; (b) stream of gas bubbles issuing from the orifice;. (c) sketch of the region around the exit orifice, showing the steady and absolutely unstable regions of the gas ligament. From [64].

(a)   (b)
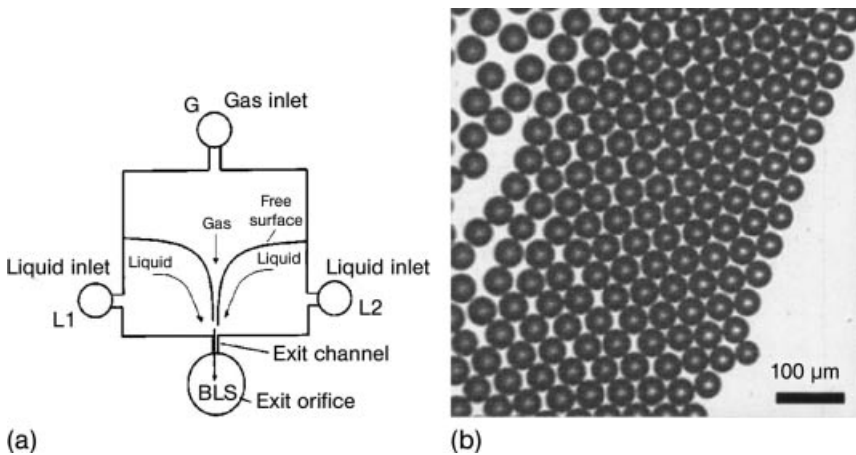
Figure 8.8 Planar flow focusing bubble generation device without nozzle. (a) Sketch of the device showing the expected shape of the free surface; (b) picture of bubble–liquid suspension obtained. From [67].
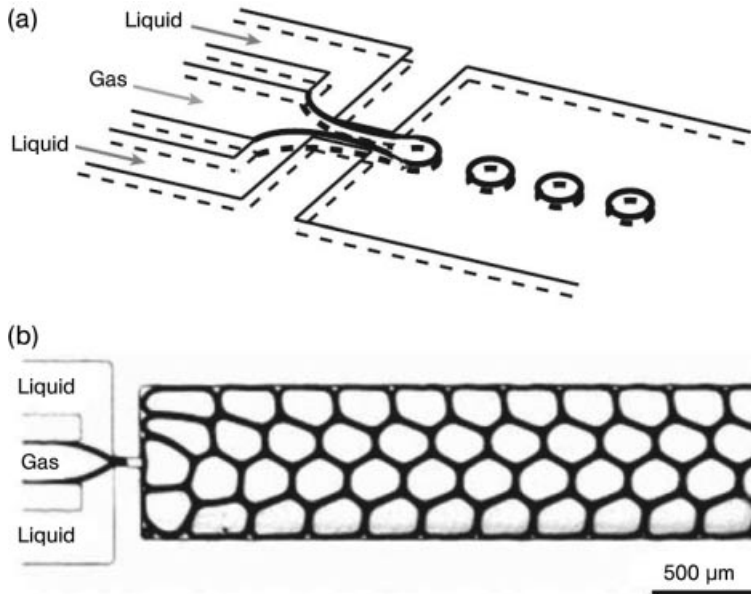
Figure 8.9 Planar flow focusing foam generation device with gas
nozzle. (a) Schematic diagram; (b) optical micrograph of the
production of a foam comprising monodisperse bubbles.
From [69].

and the orifice width was in the range 30–120 μm. Nitrogen bubbles with diameters
of 10–1000 μm in water mixtures were obtained with a polydispersity (standard
deviation of size distribution divided by average size) of <2%. The bubbles could be
generated with a frequency up to 100 kHz. At low Re, a bubble formation mechanism
similar to the *squeezing mechanism* described earlier provided good agreement with
experimental results. The bubble volume depended on the $P_g/Q_l\mu_l$ ratio but not on
interfacial tension (P_g is the gas delivery pressure). In this mechanism, the gaseous
thread advances into the constriction until it reaches the collection channel where a
bubble is inflated. As soon as the bubble is large enough to block the exit of the
constriction, the liquid squeezes the gaseous thread, forming a neck which becomes
unstable and breaks, releasing the bubble into the collection channel [70]. The thread
then retracts upstream of the orifice. The bubble formation mechanism can be
influenced by changing operating conditions and inlet geometry; the thread can
remain inside the orifice after bubble break-up and bidisperse droplets can be
formed [71, 72]. When inertial effects become important, they give rise to a rich
dynamic behavior and result in non-uniform sized bubbles at intermediate ranges of
Re and We [73].

A simple three-dimensional FF geometry can be obtained by fitting a cylindrical
capillary tube, with a constriction of 50–350 μm at its entrance, very closely into a
square capillary tube [74]. This device resulted in suspensions of nitrogen bubbles of
50–900 μm in water solutions with a gas fraction as large as 90%. The following

expression, consistent with the *squeezing mechanism* of bubble formation, provided a good fit to the experimental data:

$$\frac{d_{\mathrm{b}}}{\Omega_{\mathrm{or}}^{1/3}} = a\left(\frac{Q_{\mathrm{g}}}{Q_{\mathrm{l}}}\right)^{1/3} \tag{8.7}$$

Above the volume fraction of a two-dimensional close-packed lattice (0.91), bubbles are forced to distort their circular shapes and the flowing lattice becomes a dynamically assembled foam. A bubble influences the volume of its successors during its presence in the channel, while traveling from the orifice to the channel exit, further affecting transient behavior [75, 76]. The confinement that is inherent in microstructured devices results in a variety of periodic structures that correspond to local minima in interfacial energy, which cannot be obtained in unbounded geometries (where the only structure observed is the honeycomb lattice) [77]. The system can be switched between these structures by changes of P_{g} or Q_{l}, the transitions being accompanied by oscillations [75].

8.1.3.3 Multichannel Systems

One approach to increase foam or bubble suspension throughput is to use a multichannel system. However, issues about flow equipartition have to be carefully addressed. Mixing geometries where the number of both gas and liquid inlet channels is increased and feed into one outlet channel can employ a multilamination mixing layout. Lob *et al.* [78] utilized a variety of multilamination mixers designed for homogeneous mixing and obtained bubble suspensions with relatively low nitrogen bubble size distributions in water solutions, for low gas and liquid flow rates (Figure 8.10). Smaller bubbles were obtained with FF geometries, even though the orifice width was larger than that for the gas and liquid feeding channels. Not all channels were active for gas introduction. By increasing the gas flow rate, more gas channels became active, but this resulted in a broader bubble size distribution. To avoid flow maldistribution a three-channel design with a single gas inlet, flanked by two liquid inlets, was used and resulted in improved bubble size distribution and smaller bubbles (at the same inlet flow rates). Decreasing the distance between the mouth of the inlet channels and the orifice restricted bubble growth and resulted in smaller bubble sizes for both multichannel and three-channel mixers. A different multichannel geometry was proposed by Yasuno *et al.* [79], which is discussed in more detail in Section 8.2.2. The gas phase was introduced through 600 rectangular channels of $16 \times 4\,\mu\mathrm{m}$ cross-section into a deeper main channel where the liquid flowed. Air bubbles of size $30–50\,\mu\mathrm{m}$ in water solutions were obtained with size variations below 10%.

8.1.3.4 Dispersion Effects

When a bubble suspension generated in the mixer is fed to a large diameter "delay" tube, hexagonal close packing of bubbles is obtained (Figure 8.10). Pulses of tracer to these systems for residence time distribution determination showed that dispersion in the delay tube is negligible [80]. Dispersion increased with total flow rate and
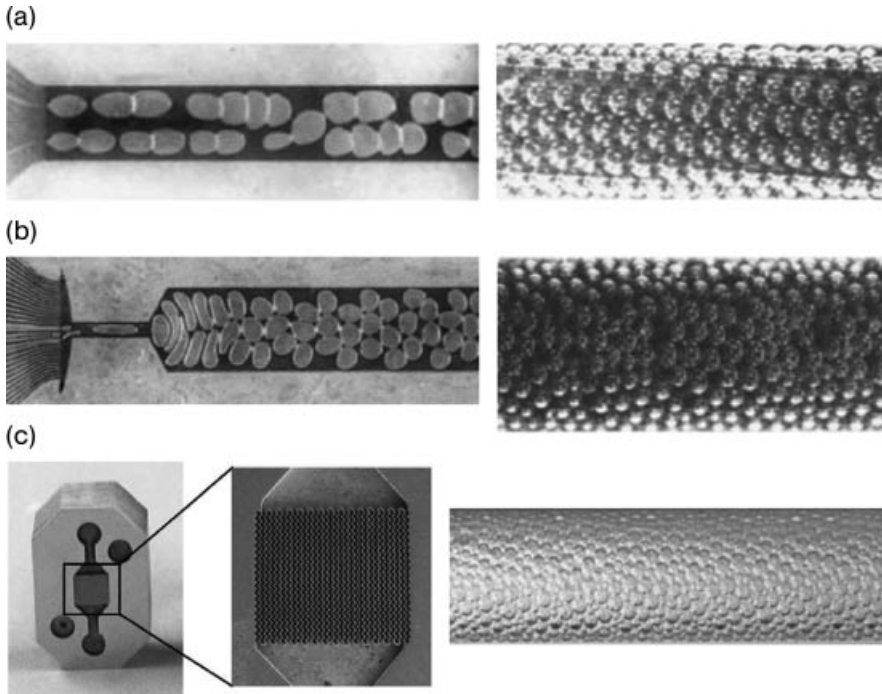
Figure 8.10 Foam formation in multichannel geometries. (a) Rectangular glass mixer; (b) slit-shaped glass mixer (flow focusing design); (c) mixing element of stainless-steel multilamination mixer, which when placed in its housing results in a 3D flow focusing mixing section similar to (b). The left images show the flow through the mixing chamber; the right images show the glass tube connected to the mixer outlet. From [78].

gas/liquid ratio and was affected by the reactor tube orientation; gravity led to up to five times higher dispersion for the vertical tube compared with the horizontal tube. A narrower bubble size distribution, which can be obtained with the three-channel mixer described above, results in lower tracer dispersion [78].

8.1.4
Overlapping Microchannel and Micromesh Contactors

In *overlapping microchannel* and *mesh microcontactors*, the two fluids (gas and liquid) flow through separate channels. To provide stable operation, the fluid interface is immobilized by well-defined openings obtained by partial overlapping of the (open on one side) channels where the two fluids flow [81] (Figure 8.11) or by a thin mesh [82] (Figure 8.12). Interfacial forces help to stabilize the fluid interface within the openings, while fluid layers are thin enough to enhance mass transfer. The overlapping microchannel contactor shown in Figure 8.11 was manufactured by anodically bonding etched silicon and glass substrates [83]. Generation of constricted
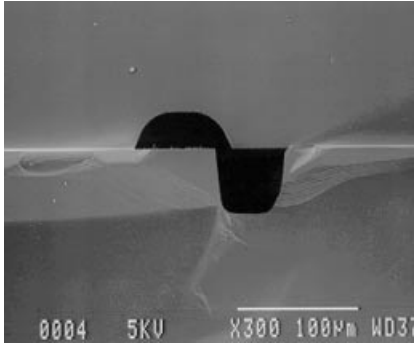
Figure 8.11 SEM image of cross-section of silicon–glass bonded
structure with overlapping microchannels to form contactor.
From [81].

openings, in the range of 5 µm, by overlapping of channels required high alignment
accuracy. A typical contactor [84] consisted of silicon with $\sim100 \times 50\,\mu m$ (cross-
section) microchannels. Due to geometric and fabrication constraints, the above
contactors had limited stability, small contact time, working volume and interfacial
area. Stability was particularly an issue for uneven pressure gradients such as those
obtained during counter-current operation. The fact that the two materials, glass and
silicon, had different wetting properties can further help in stabilizing the interface,
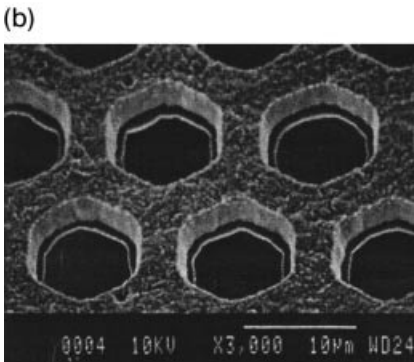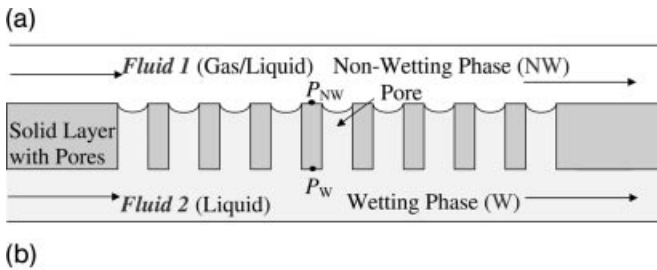
Figure 8.12 Micromesh contactor. (a) Schematic
representation of contacting of immiscible fluids; (b) SEM
image of pores of a nickel micromesh. From [82].)

not only by flow confinement but also by wetting mismatch between the two channels. Another way of inducing this wetting mismatch is by selectively coating one of the channels with a hydrophobic coating such as octadecyltrichlorosilane [85]. Mesh or porous plate microcontactors can alleviate some of the problems encountered in overlapping channel contactors [82, 86]. Wenn *et al.* [82] implemented a mesh structure to separate planar chambers containing the two fluids (Figure 8.12). The mesh to wall distances could be set generally to ~100 μm, while the pore widths were typically ~5 μm and provided adequate stability. A pore length (mesh thickness) to width ratio of ~1:1 ensured low diffusive transport resistance through the mesh. The latter was placed between two glass layers that form chambers for the two fluids. The mesh was fabricated in nickel using photolithography and a two-stage electroplating method.

The meniscus shape at the interface between the two phases defines the available area for mass transfer and is a function of contact angle, pore geometry and pressure difference between phases. The open area of the micromesh contactor was about 20–25%, which leads to a gas–liquid interfacial area of $2000\,m^2\,m^{-3}$, well above the values obtained in traditional stirred tank reactors. This high gas–liquid interfacial area combined with the small fluid layer thickness resulted in high mass transfer coefficients. Values of volumetric mass transfer coefficients, $k_L a_L$, during hydrogenation of up to $\sim 2\,s^{-1}$ have been measured experimentally [87]. These contactors also have other advantages, such as lower pressure drop and no danger of flooding compared with bubble or packed columns. The fluids should be free of particulates to avoid fouling of the pores. Operation of such overlapping channel or mesh devices requires that the pressures utilized to drive flow do not produce excessive differential pressures across the opening. Breakthrough of one phase into the other is broadly predictable by the Young–Laplace expression

$$\Delta P = \frac{\gamma \cos\theta}{R} \quad \text{for slot}$$

$$\Delta P = \frac{2\gamma \cos\theta}{R} \quad \text{for circular opening} \tag{8.8}$$

For more precise evaluation of breakthrough limits, dynamic contact angles and meniscus contortion at the pore mouth(s) must also be considered [88]. The Young–Laplace equation can still be used to determine the stability of the system for straight cylindrical pores with rounded edges using $\theta_A + 90°$ for breakthrough of the wetting in the non-wetting phase and $0°$ for breakthrough of the non-wetting in the wetting phase (θ_A is advancing contact angle). In practice, although narrower openings provide greater stabilization, observed pressure differentials for breakthrough tend to be somewhat lower than predicted.

8.1.5
### Falling Film Microchannel Contactor

Falling film contactors employ thin liquid films that are created by a liquid feed falling under gravitational pull. The liquid film is in contact with a solid support, which is
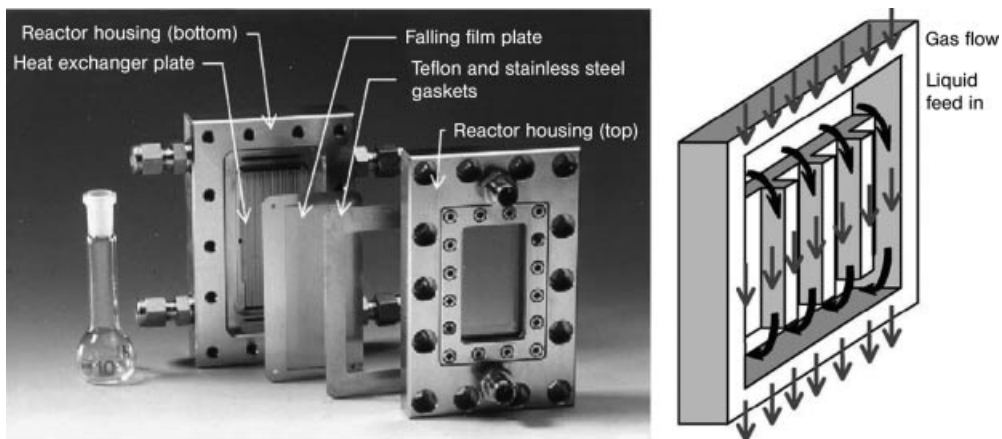
Figure 8.13 Disassembled falling film microchannel contactor and schematic showing the gas–liquid contacting. From [92].

usually either a thin wall or stack of pipes. Conventional falling film systems generate films with thickness of the order of 0.5–3 mm [89]. At high flow rates, the film takes the form of continuous sheets, which may demonstrate waviness. At either the front end of those sheets or at low flow rates, flow breaks up into rivulets, fingers or a series of droplets [90]. A falling film microchannel contactor [91, 92] developed by the Institut für Mikrotechnik Mainz (Figure 8.13) can generate stable films less than 100 μm thick. The most critical part of the contactor is the stainless-steel plate where the falling film is generated. Open microchannels (typically 300 μm wide, 100 μm deep, separated by 100 μm wide walls) are fabricated using electrodischarge machining or wet chemical etching. Supply and withdrawal of liquid are through boreholes which are connected via one large slit to numerous small orifices at the top of the microchannels. The slit acts as flow restrictor and aids the equipartition of the liquid phase to parallel streams. The entire plate is housed in a stainless-steel enclosure and a structured heat exchanger copper plate is inserted into a cavity beneath the falling film plate for temperature control. When both top and bottom parts of the housing are placed together, a cavity is created above the plate through which the gas flows.

The function of the microchannels is to prevent break-up of the liquid film. Due to the combination of capillary forces and small channel widths, liquid being pulled up along the sides of the channels takes up a significant portion of the channel width and the surface of the liquid film takes the form of a flowing meniscus. At low flow rates, the surface of the film curves upwards while moving from the center of the channel to the walls [93]. As the flow rate increases, the film thickness increases and the surface profile becomes flatter. Further increase in the flow rate causes the liquid to bulge out of the channel until hydrostatic pressure exceeds surface tension forces and the liquid bursts out of its channel wall confines. The film thickness observed for various microchannel sizes was mostly smaller than the Nusselt and Feind equations, while the Kapitza equation gave the closest overall prediction (Figure 8.14).
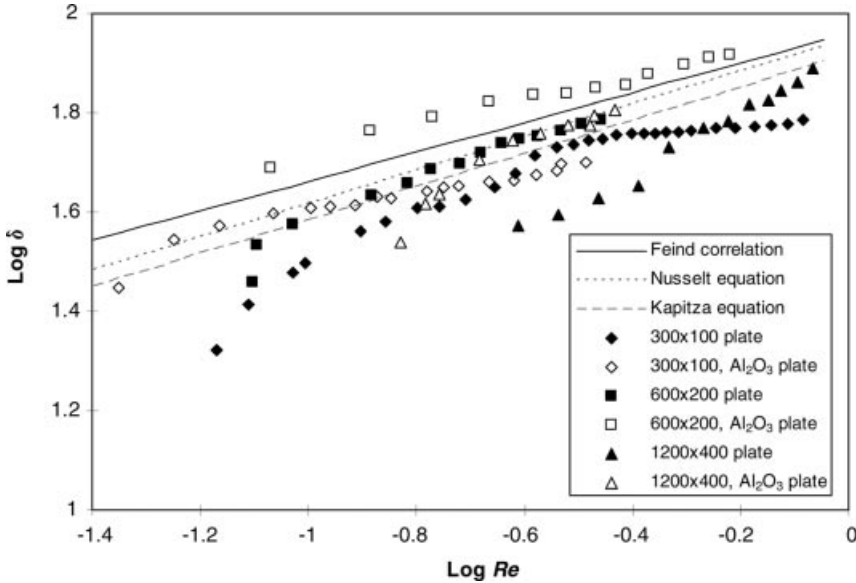
Figure 8.14 Relationship between liquid film thickness, δ, and
Reynolds number, *Re*, obtained experimentally (points) and
theoretically (lines) (liquid ethanol). From [93].

$$\text{Nusselt}: \quad \delta = \left(\frac{3\nu^2 Re}{g\sin\theta}\right)^{1/3} \tag{8.9}$$

$$\text{Kapitza}: \quad \delta = \left(\frac{2.4\nu^2 Re}{g\sin\theta}\right)^{1/3} \tag{8.10}$$

$$\text{Feind}: \quad \delta = \left(\frac{3\nu^2}{g\sin\theta}\right)^{1/3} Re^{0.333\nu'^{-0.11}} \, \nu'^{0.025} \tag{8.11}$$

However, existing correlations are for two-dimensional films and do not account for three-phase contact and surface tension. Hence they cannot capture the effect of microchannel width on falling film thickness. A specific interfacial area of ∼20 000 $m^2\,m^{-3}$ can be achieved with this contactor. This is larger than conventional bubble columns and agitated tanks (up to 200 $m^2\,m^{-3}$) [94]. In spite of the small film size, axial dispersion can be present [95]. Depending on the channel cross-section (which in turn depends on the microstructuring method utilized), the cross-sectional velocity profile displays a single (for rectangular microchannels made by electrical discharge machining) or a double maximum (for rounded corners microchannels made by wet chemical etching). For nitrobenzene hydrogenation, an overall mass transfer coefficient (based on liquid volume) $k_L a_L$ of 3–8 s^{-1} was estimated [96]. Reducing the flow rate and therefore the liquid film thickness increases the $k_L a_L$ values. However, the need to avoid liquid film dry-out imposes a minimum practical

Figure 8.15 Disassembled and partially assembled helicoidal microchannel falling film contactor with path length 540 mm. From [97].

flow rate. Decreasing the flow rate results in an increase not only in residence time but also specific interfacial area.

One of the limitations of the falling film contactor is that the residence time of the liquid in the microchannel is ~5–20 s, the exact value depending of the liquid properties and operating conditions. This can be increased by increasing the microchannel length. Another way is to decrease the angle of descent, which can be achieved with the helicoidal microchannel falling film reactor (Figure 8.15). In this case, the microchannel has a small angle descend of 7.5°, resulting in an increase in residence time by a factor of 50 [97]. Scaled-up versions (by a factor of 10) of the falling film contactor have been designed and evaluated [98]. This was accomplished by either increasing the number and the length of the microchannels in a planar format or placing the vertical channels in a cylindrical configuration. Similar levels of reaction performance were obtained in the scaled-up reactors as compared with the standard version (Figure 8.13), as demonstrated with a liquid-phase oxidation and CO_2 absorption. During scale-up, care must be taken to avoid liquid flow maldistribution and undesired gas recirculation patterns [99].

8.2
Non-miscible Liquid–Liquid Systems

In liquid–liquid flows, wettability phenomena can significantly affect the flow patterns formed as both fluids, unlike in gas–liquid flows, can wet the channel wall. In addition, neither phase has negligible viscosity and both phases are incompressible. Dreyfus *et al.* [100] demonstrated that ordered patterns in liquid–liquid flows could only form when one phase completely wets the channel wall (Figure 8.16a), while disordered not well-defined patterns form, with phases adhering intermittently to the channel walls, when wetting is partial (Figure 8.16b). Xu *et al.* [101] obtained slug flow only when the continuous phase fully wetted the channel wall and for other cases poorly defined flow configurations occurred. Although for complete wetting
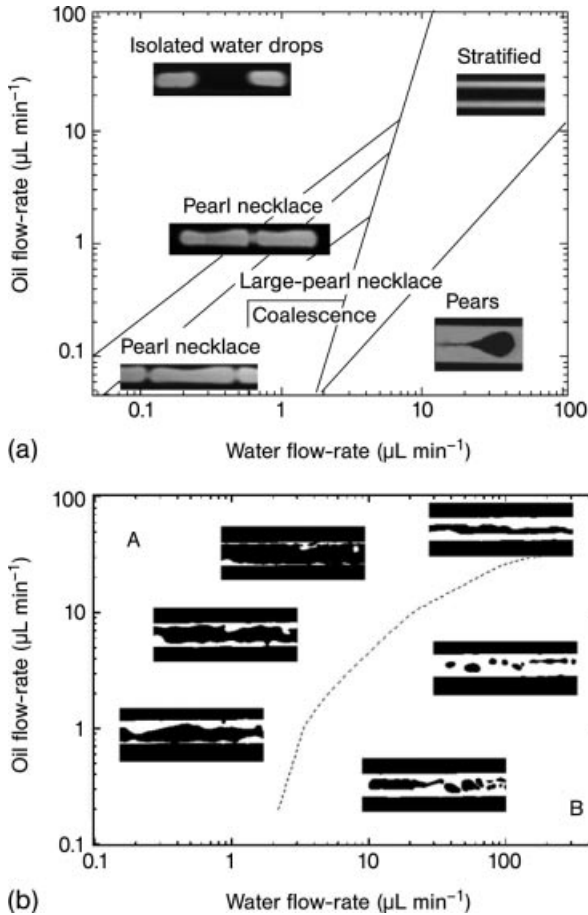
Figure 8.16 Flow patterns during water and tetradecane with surfactant (SPAN 80) flow in silicon–glass microchannels with 20 × 200 μm cross-section. (a) Organic phase completely wets the silicon channel wall at surfactant concentration 2.2% w/w; (b) no surfactant is used and the organic phase partially wets the channel wall. From [100].

surfactant has to be added at a concentration above the critical micellar concentration (CMC), the change from disordered to ordered patterns occurred at concentrations an order of magnitude above the CMC [100]. Decreasing the channel size also tends to favor disordered patterns. A flow pattern map that combined data by a number of investigators was given by Günther and Jensen [2] (Figure 8.17). Hydrophobic surfaces are obtained with soft-lithographically patterned PDMS devices, whereas microchannels patterned in silicon, glass and metals have various degrees of hydrophilicity and would have to be treated or surfactants need to be added so that walls are fully wetted by one or the other phase. A criterion was suggested by Guillot and Colin [102] to predict the transition from slug to stratified flow at high dispersed
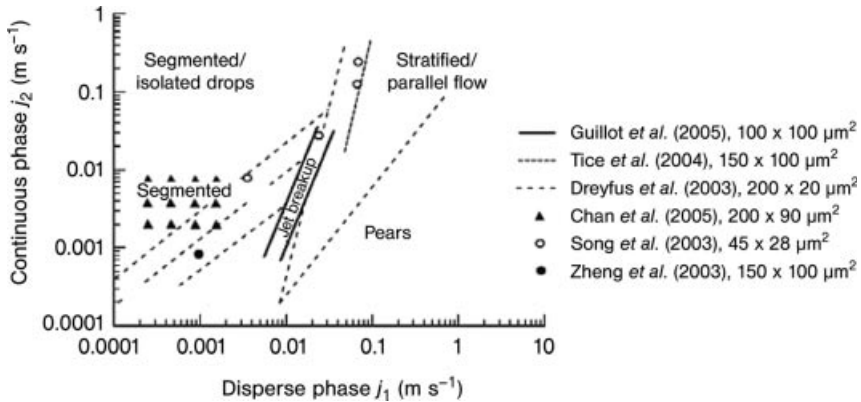
Figure 8.17 Flow pattern diagram for liquid–liquid flows in microfabricated systems with transition lines from different literature data. From [2].

phase fractions, that was based on the "squeezing" formation mechanism described in Section 8.1.1.1 and discussed below for liquid–liquid flows.

8.2.1
Segmented Flow Contactors

In the segmented pattern during the flow of two immiscible liquids, depending on wall wettability, either phase can be the continuous one in contact with the channel wall. We will call the continuous phase segments "slugs" and the discontinuous phase segments "plugs". Plugs are equivalent to bubbles in Taylor flow. Flow circulation patterns appear both within the slugs and the plugs. Liquid-phase reactions can be carried out in the plugs, thus reducing axial dispersion and avoiding direct contact with the channel wall, thereby eliminating any contamination or clogging of microchannels due to deposition of material on wall surfaces. In this case, the second fluid is introduced for the purpose of improving mixing and reducing axial dispersion. Their isolation allows plugs to be used as individual batch reactors in high-throughput analysis or synthesis.

8.2.1.1   Slug/Plug Formation
Segmented liquid–liquid flow has been produced with a number of different inlet configurations. The dispersed phase plug length does not seem to depend on the balance of shear (viscous) and interfacial stresses and therefore on *Ca* as is the case with drop formation (see Section 8.2.2). Rather, the "squeezing" mechanism, as described in Section 8.1.1.1 for gas–liquid flows, applies where plug formation and size are determined by the competition between Laplace forces and the force related to the resistance to flow of the continuous fluid by the emerging drop. For T-junctions where the dispersed fluid enters from the side channel, Equation (8.1) can be used. When $Q_c \gg Q_d$, the plug size is constant and equal to channel width, whereas when

$Q_c < Q_d$ the plug size depends on the ratio of the flow rates of the two liquids. According to Garstecki *et al.* [25], the mechanism is valid for dispersed phase inlet channels with width at least equal to half the width of the main channel, where the emerging dispersed phase can block the main channel. For a smaller dispersed phase inlet, the drops are smaller than the main channel and shear forces become important. A similar mechanism was suggested by Guillot and Colin [102] for a funnel-type inlet, where the two liquids entered in an almost stratified manner. Thorsen *et al.* [103] found that in a T-junction even with similar size main and dispersed phase channels, *Ca* affects the plug size when the forming dispersed phase does not block the main channel. Tice *et al.* [104] suggested that shear forces and *Ca* affect drop size for *Ca* > 0.1. For lower *Ca*, plug length depended on the relative flow rates of the two liquids but not on total flow rate and therefore on *Ca*, while the data were correlated with the phase fraction. No dependence of plug length on total flow rate was also found by Xu *et al.* [101], who, however, suggested a correlation with Q_d/Q_c different to Equation (8.1); in their case, the dispersed phase entered from the main channel. For large *Ca*, Adzima and Velankar [105] measured plug lengths that were inconsistent with Equation (8.1) but could be related to phase fraction. In contrast to the above, Burns and Ramshaw [106] found in a T-junction where the two phases entered from opposite sides that plug lengths depended on total flow rate.

In a cross-flow inlet configuration, Zheng *et al.* [107] observed that drops of the dispersed phase formed alternatingly from each of the two opposite dispersed phase inlet channels (Figure 8.18). At low dispersed phase fractions, there was a wide range of *Ca* where this mechanism appeared, but at dispersed phase fractions above 0.6, this was not possible.
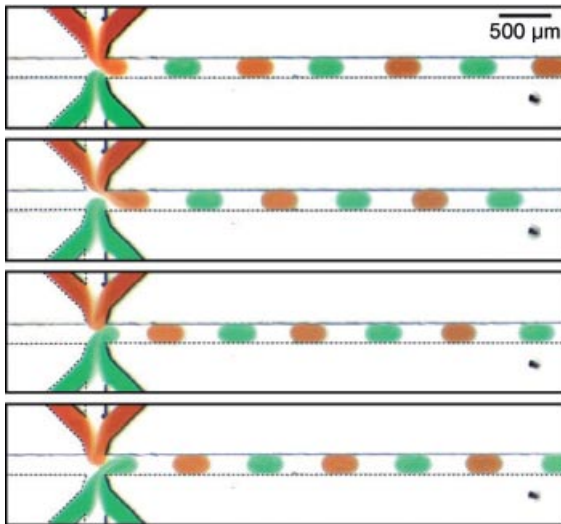
Figure 8.18 Formation of alternating plugs during liquid–liquid flow in a cross-flow inlet configuration. From [107].

8.2.1.2 **Hydrodynamics and Mixing**

The flow field inside the slugs and plugs has been investigated by CFD modeling and PIV measurements. Normalized circulation times in both slugs and plugs were found to be about 3–4, which means that a fluid element within a slug or plug will move from one end to the other during the time the slug/plug has traveled a distance 3–4 times its own length. These times remained almost constant with increasing flow velocity apart from the case of slugs shorter than the channel diameter and no film on the wall [108]. Mixing times within plugs, half of which contained solute, were found to be much smaller in the convection than the diffusion dominating regime [109]. Convection dominates over diffusion when the plug velocity is much larger than a critical velocity, where the diffusive time-scale equals the convective one; the opposite happens at velocities lower than the critical value. Increased flow (and consequently drop) velocities were found to improve conversion in nitration reactions occurring within aqueous plugs, which was attributed to improved mass transfer [110].

Reagents can be added to already formed segmented flow plugs by side channels in T-junctions. The reagent can be added directly into the plug when the side channel wall is wetted by the plug phase, otherwise Ca should be low. Another injection method is to use side channels that are preferentially wetted by the reagents that need to be added. A droplet forms from the injection of the reagent that remains on top of the side channel inside the main channel because the wetting of the side channel prevents the droplet from breaking away. This droplet will only be broken off by and join a passing plug [111]. The possibility of forming plugs alternatingly from the two side inlets in a cross-flow configuration [107] has been used for indexing, where the concentration of a solute in a plug is measured by the addition of a marker in an adjacent plug. Reagent concentrations within plugs can also be varied by combining streams of reagents with buffer solutions in the inlet channel of the phase that forms the plug. Following the same approach, different reagents can be added in the plug, in which case the plug acts as a small reactor. The way in which the reagents are added in the plug can, however, affect their mixing [104, 112].

As in gas-liquid flow, serpentine channels have also been used in liquid–liquid segmented flow to improve mixing within plugs [113]. Mixing is achieved through chaotic advection, which relies on repeated folding and stretching of fluid layers with different concentrations that become thinner and thinner until mixing by diffusion becomes rapid (Figure 8.19).

8.2.1.3 **Pressure Drop**

Pressure drop in an organic–aqueous segmented flow, with water forming the dispersed plugs, was found to be higher than organic single-phase flow at the same total velocity and to increase with plug size, even though the water had a lower viscosity than the organic phase [105]. Uncoated channels with walls partially wetted by the phases showed a higher pressure drop than channels fully wetted by the organic phase; this increase was attributed to the moving water/organic contact lines in the non-fully wetted channels.
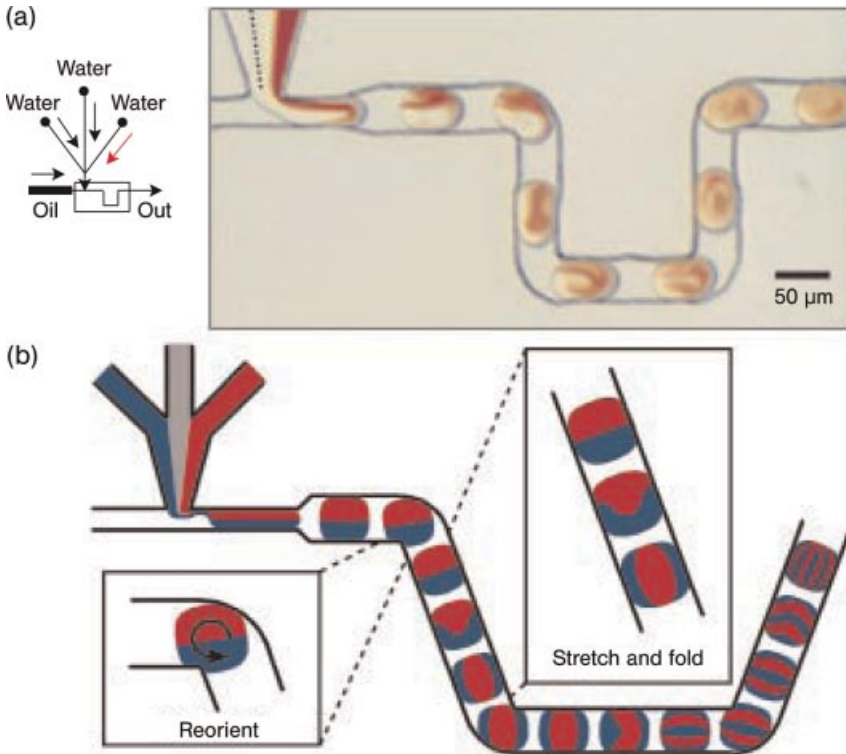
Figure 8.19 Mixing within liquid plug in a serpentine microchannel (a) experimentally; (b) schematically. From [113].

8.2.2
Liquid–Liquid Dispersion Microcontactors

The generation of liquid–liquid dispersions, commonly used as emulsions, has many commonalities with the generation of bubble suspensions, but differences also exist, due to the different ranges of interfacial tensions, viscosities and densities between the two systems. Surfactants are often introduced to facilitate dispersion formation and reduce coalescence.

8.2.2.1 T-type and Co-flow Mixing Section Geometries
Liquid–liquid dispersions can be produced in T-junctions feeding to a larger collection channel. The mixing geometry forces the two flows of immiscible liquids to merge in such a way that one liquid forms droplets dispersed in the other. The dispersed phase can be selected by adjusting the wetting properties of the device walls. This can be achieved by coating the channels with hydrophilic/hydrophobic compounds or introducing surfactants in the continuous phase [114]. The relative flow rates of the two liquids can be utilized to adjust droplet size. These are the main parameters that affect droplet size in the pressure-dominated *squeezing regime*.
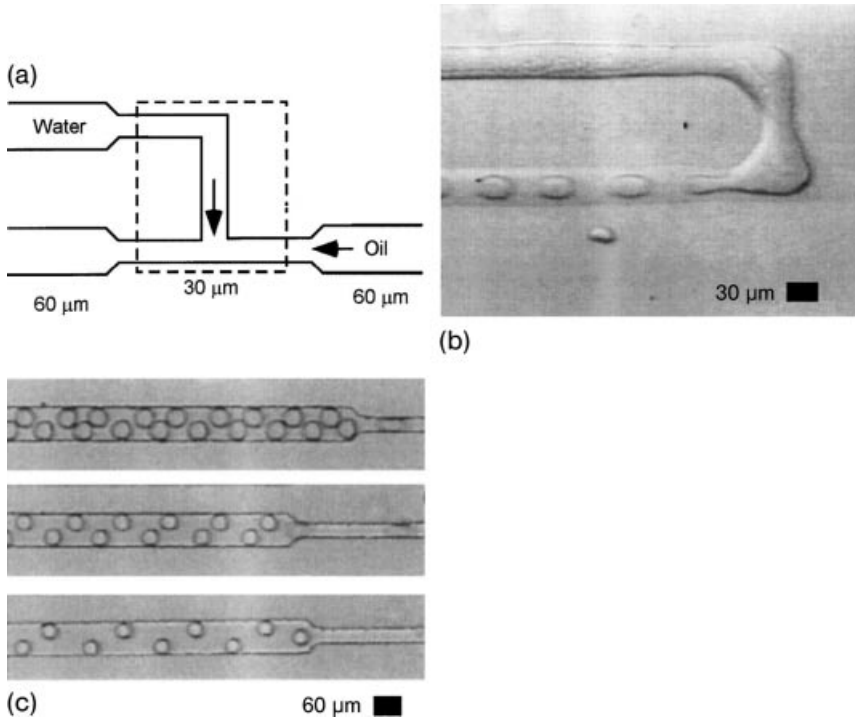
Figure 8.20 Microchannel T-junction for formation of liquid–liquid dispersion. (a) Junction schematic [dashed rectangle indicates area in (b)]; (b) photomicrograph of the discontinuous water phase introduced into the continuous oil phase; (c) droplets in square channels. Photomicrographs show the transition from the 30 μm wide channel to the 60 μm wide channel. From [103].

Thorsen *et al.* [103] generated water in oil–surfactant dispersions in a T-junction as shown in Figure 8.20. Monodisperse droplets with a size similar to that of the T-junction channels were formed at generation frequency of 20–80 Hz. With smaller inlet size for the dispersed phase, shear stress can distort the forming droplet, leading to droplets smaller in size than the outlet junction channel characteristic width [25, 115], as shown in Figure 8.21. When the droplet is smaller than the smallest dimension of the outlet mixing channel, wall effects play a diminishing role and the system behavior approaches that obtained in unbounded flow. In shear flows, droplet break-up is affected not only by *Ca* but also by the ratio of the viscosities of the two phases. When inertial effects can be neglected, drops break above a critical *Ca* [116, 117] and their size is inversely proportional to *Ca* [101, 118, 119]:

$$\frac{d_{\mathrm{d}}}{d_{\mathrm{in,d}}} = a Ca^{-1} \tag{8.12}$$

However, when the droplet diameters are large, wall effects become important and the dependence of droplet size on *Ca* becomes weaker, $d_{\mathrm{d}} \sim Ca^{-0.3}$ [118–120].
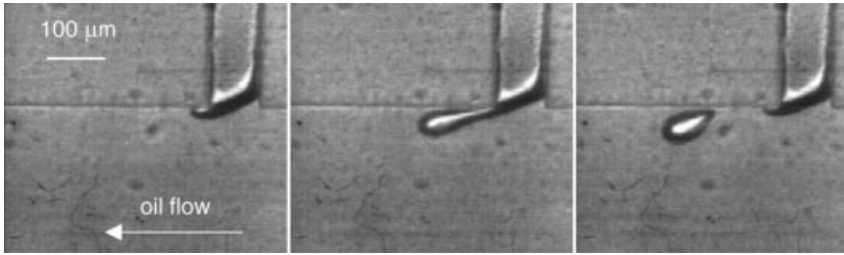
Figure 8.21 Droplet formation at T-junction. The channels have a depth of 100 μm. The dispersed inlet flow enters through a 100 μm wide channel, while the continuous phase flows in a 500 μm channel. From [115].

Various approaches have been proposed for liquid–liquid dispersion generation in unbounded flows using small openings for dispersed phase introduction. Drops form at the opening and detach when they reach a size when streamwise forces exceed interfacial tension forces. A cross-flow configuration based on a microstructured silicon device with a single square hole of 45 × 45 μm [121] produced droplets of ∼150 μm for a butanol–water system. Another one with a 4.8 μm circular opening produced aqueous solution droplets of ∼35 μm. The size decreased with decreasing pressure of the dispersed phase [122].

For co-flow, the *dripping* (where the drops form close to the dispersed phase inlet mouth after break-up of the connecting neck) and *jetting* (when the drops break up from an extended liquid jet due to Rayleigh instabilities) regimes are encountered. The dripping regime which occurs at low dispersed and continuous phase flow rates and low viscosity ratio of dispersed to continuous phase, provides stable droplet growth, leading to size uniformity, but it may also exhibit bidisperse or polydisperse droplet distributions [123, 124]. Cramer *et al.* [123], using a tube-in-a-tube configuration with a 20 μm inner tube inlet, generated droplets of <35 μm and achieved a generation frequency of 5 kHz and less than 1% polydispersity. Umbanhowar *et al.* [125] introduced the dispersed phase through a 0.7–100 μm capillary tip in a surfactant containing continuous phase which was placed in a rotating cup, so that the free surface was almost vertical. This device generated 2–200 μm droplets with polydispersity <3%. A simplified model, accounting for drag and interfacial forces and applicable to large *Re* (0.1–100), showed that the critical parameter was *Ca*:

$$\frac{d_\mathrm{d}}{d_\mathrm{in,d}} = a + bCa^{-1} \tag{8.13}$$

The above equation does not account for the droplet size increase due to fluid transfer through the neck during droplet detachment and hence does not capture the fact that increasing the flow rate of the dispersed phase leads to a larger droplet size [123]. A force balance analysis accounting for this effect, and also other detaching forces, can provide a more accurate prediction of droplet size [121].

8.2.2.2 **Flow Focusing Geometries**

Liquid–liquid dispersion can be created using flow focusing (FF) devices similar to those described in Section 8.1.3, with two streams of one liquid flanking a stream of a second immiscible liquid, the combined two-phase flow then being forced through a small orifice. The pressure and viscous forces exerted by the outer fluid force the inner fluid into a narrow thread, which then breaks into droplets inside or down-stream of the orifice. For a planar FF device (Figure 8.9a), with orifice width ~40 μm and channel depth ~100 μm, various droplet formation mechanisms including *dripping* and *jetting* were observed on changing the flow rates of the oil continuous phase and water dispersed phase at $Re < 18$ (Figure 8.22) [126–128]. At low flow rates, nearly monodisperse droplets whose size was comparable to the orifice width were obtained. High flow rates allowed the formation of monodisperse droplets with high frequencies (<10 kHz), whose size was much smaller than the orifice width. Bidisperse and polydisperse droplet size distribution was also encountered (see also [120, 129]). The presence of surfactant could lead to a conical shaped interface with a highly sharpened tip. Tiny liquid threads and micrometer sized droplets streamed off the end of this tip, either continuously (high Q_c/Q_d) or alternating with large droplets (low Q_c/Q_d). The process resembled tip streaming, reported for large isolated droplets in unbounded linear flow [117].
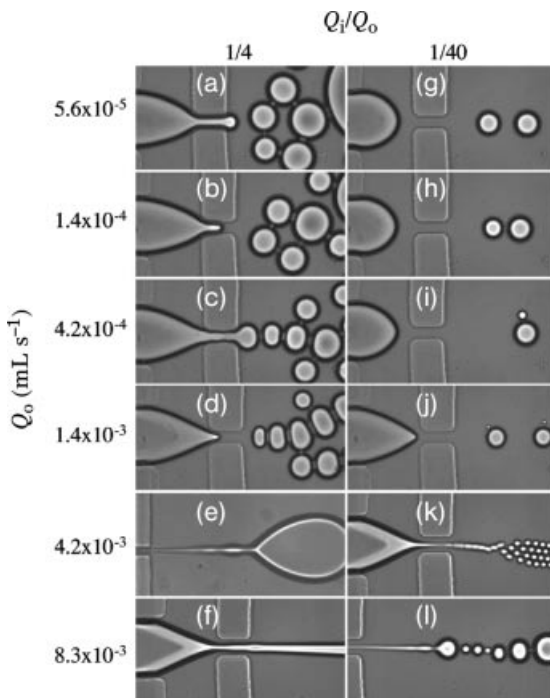
Figure 8.22 Pictures of drop formation in flow focusing device at different values of the continuous Q_o and dispersed phase Q_i flow rates. From [126].

In the above planar device, when the drop is of comparable size to the orifice, it may be squeezed by the top and bottom walls. This leads to shear and possible damage but can be avoided by three-dimensional FF geometries. Takeuchi *et al.* [130] fabricated an axisymmetric device with a 250 μm orifice by casting PDMS around locally shaved optical fibers. By increasing the flow rate of the continuous hexadecane solution, the size of aqueous droplets decreased. Droplet size in the range 50–300 μm with frequency ∼10 Hz were obtained. Yobas *et al.* [131] used silicon micromachining to fabricate a circular 24 μm diameter and 16 μm long constriction directly inside the FF geometry. Oil droplets as small as 25 μm and formation frequencies of 900 Hz were obtained. The diameter of water droplets generated in the dripping regime were proportional to Q_c^{-1}. In the jetting regime, the droplet size could be reduced to 10 μm and frequencies exceeded 10 kHz.

In the *jetting regime*, where inertial forces become important, droplet uniformity decreases somewhat but the frequency of generation and hence throughput can be increased, while droplets with smaller size than the orifice can be produced. In a planar FF geometry, similar to that in Figure 8.9a, Nie *et al.* [132] obtained <100 μm monodisperse droplets (within 2.5%) with an orifice 60 μm wide and 200 μm high at intermediate ranges of *Re* (∼100). At even higher *Re* (∼500), Martin-Banderas *et al.* [133], using a device similar to that shown in Figure 8.7, obtained droplets as small as 5 μm, 1/10 to 1/30 of the orifice diameter (100–200 μm). Polydispersity was slightly higher at 10%, but a droplet generation frequency up to 1 MHz was achieved. Droplet size in the jetting regime increases with Q_d and decreases with Q_c and can be predicted by a simple model of the Rayleigh hydrodynamic instability [132, 133].

With the above devices, the droplet size is controlled by changing the flow rates of the phases. However, it may not be possible to control independently dispersed phase volume fraction and droplet size. An alternative approach is to form large droplets at the required volume fraction and then break them up to the required size, without altering the dispersed phase volume fraction. This can be achieved through instabilities induced in extensional flows by passing droplets through contractions [134] or T-junctions [135]. Using a sequence of T-junctions, droplets progressively break to a size of the order of the channel width (Figure 8.23). Deformed droplets with length larger than their circumference always break at T-junction consistently with a Rayleigh-plateau instability, even though they may be stabilized at straight channels due to wall-induced distortion of the shear flow field [136]. Deformed droplets break at T-junctions above a critical *Ca* given by [135, 137]

$$Ca = a\varepsilon_0 \left(\frac{1}{\varepsilon_0^{2/3}} - 1 \right)^2 \tag{8.14}$$

8.2.2.3 Multichannel Systems

Increased throughput can be obtained by using multichannel geometries, but the droplet size distribution may become broader. Various planar and three-dimensional interdigital mixers, with or without focusing, were investigated for water–oil and
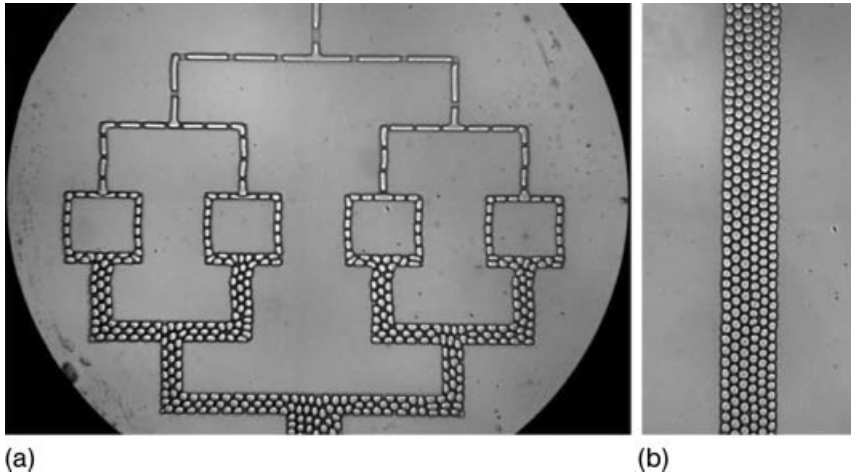
Figure 8.23 (a) Droplet break-up in sequential T-junctions; (b) the droplets flow downstream with hexagonal-close-packed ordering. From [135].

water–heptane systems (Figure 8.24) [138–140]. The geometry of the mixing section affected the droplet formation mechanism. For the non-focusing geometry, at low total flow rates droplets formed at the exit of the feed channels and led to droplets significantly larger than the feed channel width. A higher total flow rate led to the formation of jets that broke to droplets after a certain length due to Rayleigh-plateau instability. An increase in the total flow rate (at constant flow rate ratio) increased the length of the jet to the point that no decay of the jet could be observed in the outlet mixing channel. Interaction of the jets with the channel walls improved jet stability [141]. Altering the ratio of the two flow rates could be used to reverse the dispersed phase; the phase with the lower flow rate became the dispersed phase. If this was the non-wetting phase, the drops were formed from cylindrical jets, whereas when it was the wetting phase, the jets were thin lamellae in contact with the top and bottom walls. For the focusing geometries, droplet formation was influenced by shear forces and vortex flows as indicated by the presence of eddies (Figure 8.24). An increase in the total flow rate (at constant flow rate ratio) significantly decreased the droplet size and narrowed the droplet size distribution. Decreasing the size of the feed channels for the 3D mixers to 25 μm reduced the average droplet size to >5.6 μm, whereas decreasing the distance between the mouth of the inlet channels and the orifice and the number of feeding channels also resulted in a smaller droplet size and narrower drop size distribution. Droplet size correlated with energy input; small drops were obtained at high energy input.

A few devices have been proposed that resemble cross-flow membrane emulsification, where a phase is induced to disperse through the small openings of a membrane in a flow of continuous phase [3]. Such processes are more energy efficient than conventional approaches such as colloid mills and homogenizers [142]. A microstructured analogue of membrane emulsification was presented by de
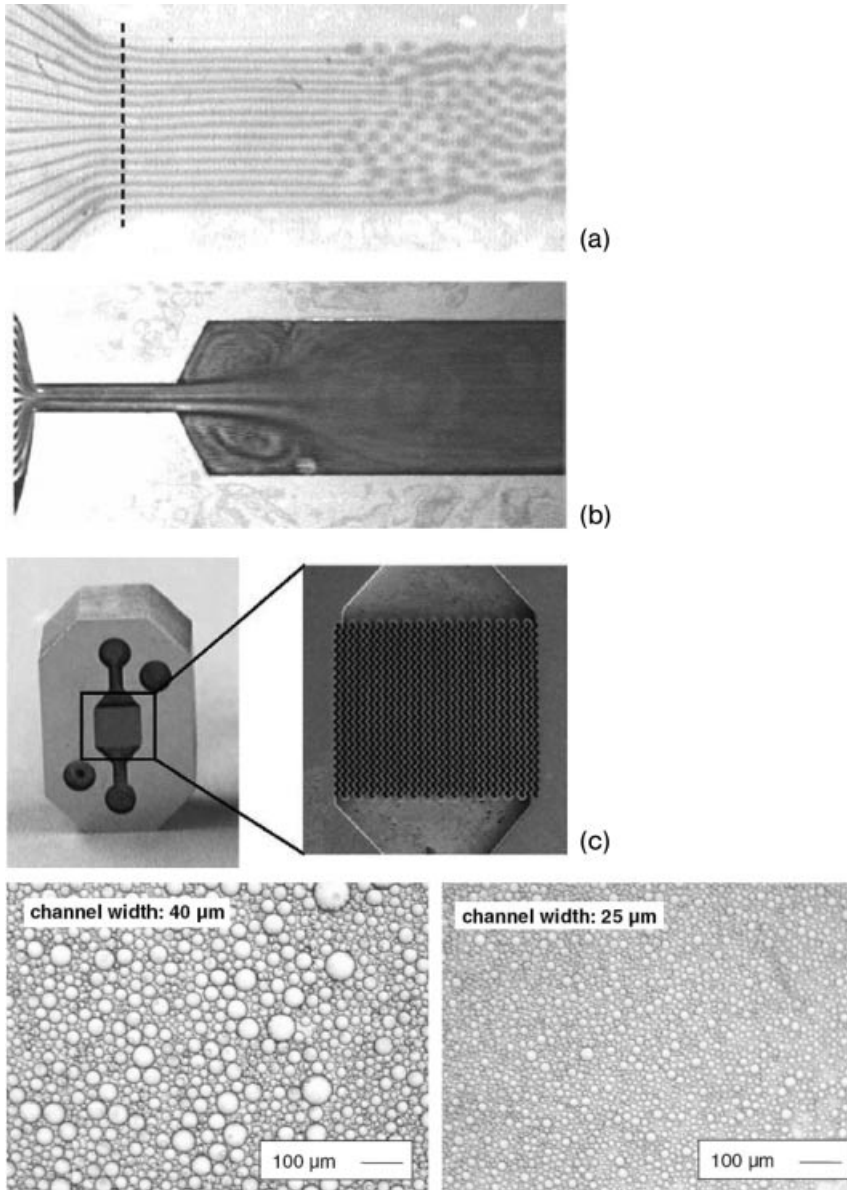
Figure 8.24 Liquid–liquid dispersion generation by multichannel devices with (a) planar non-focusing mixing chamber; (b) planar focusing mixing chamber; (c) 3D focusing mixing chamber geometry (obtained when the mixing element shown is placed in an appropriate housing). From [140].

Jong *et al.* [143]. Porous microfluidic devices were fabricated by phase separation micromolding. Oil-in-water emulsions with 190 μm size and polydispersity 2.5% were produced inside 150 μm diameter porous microchannels. Sugiura and co-workers [144–148] proposed a microfabricated silicon geometry containing at least 400 microchannels of small dimensions (typical cross-section 6 × 13 μm) (Figure 8.25). Not all the channels were initially active, but as the pressure of the
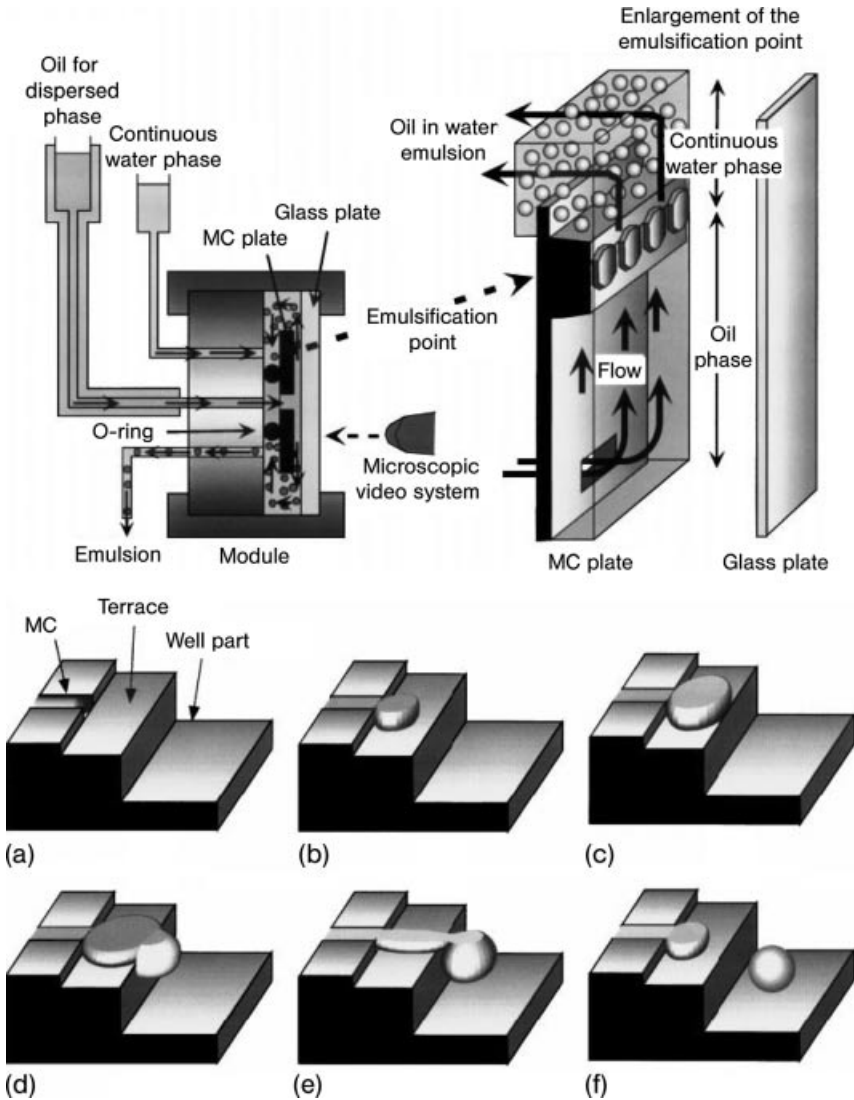
Figure 8.25 Microchannel emulsification set-up and device incorporating a stepped terrace, and steps of the drop formation mechanism: (a–c) inflation stage; (d–f) detachment stage. From [144].

dispersed phase increased above the breakthrough pressure, more channels, up to 100%, became active. Slit-like terraces placed at the exit of the microchannels were important for stable droplet production and uniformity. They induced spontaneous transformation of disk-like droplets (with higher Laplace pressure) to spherical droplets, driven by interface free energy minimization. Droplet formation occurred by a slow inflation stage at the terrace, followed by a faster detachment process. At low *Ca*, when interfacial forces were dominant, small oil droplets were formed (typically 20 μm diameter with <5% polydispersity). Their size was independent of channel width, flow velocity and interfacial tension, while small terrace length and micro-channel depth resulted in smaller droplets. Above a critical *Ca*, larger droplets were obtained. It was important that the dispersed phase did not wet the walls, in order to ensure droplet size uniformity. Even though the droplet formation frequency per channel was <15 Hz, a device containing 1500 channels could achieve frequencies of ~20 kHz. With even smaller channels (cross-section 0.3×3 μm). oil droplets with size ~1 μm and polydispersity ~10% could be produced [149]. Similar beneficial effects (in terms of drop size and phase fraction control) of altering the droplet formation mechanism by introducing an abrupt expansion in the flow were reported by Priest *et al.* [150] and Chan *et al.* [151]. A slightly different configuration is that of short channels that can be obtained in microsieve structures. Emulsification in devices containing silicon nitride microsieves with pores of 7 μm diameter and 1 μm length produced polydispersed droplets of water solution in the range 50–250 μm [152]. The droplet diameter decreased with increasing pressure of the dispersed phase, because this increased the number of active pores leading to the droplets hindering each other during growth. Droplet generation frequencies per pore were of the order of 1 Hz. Because silicon nitride is hydrophilic, hydrophobic coatings were applied for stable water-in-oil emulsification [153]. In a slightly different design, microchannels were etched through a 200 μm thick silicon wafer (Figure 8.26) [154, 155]. With oblong openings of 17 μm equivalent diameter, the droplet size was 32 μm and was independent of cross-flow velocity and transmem-brane pressure. For 10 μm circular openings, droplet formation depended on these parameters and the droplets were ~100 μm. More importantly, the oblong channels
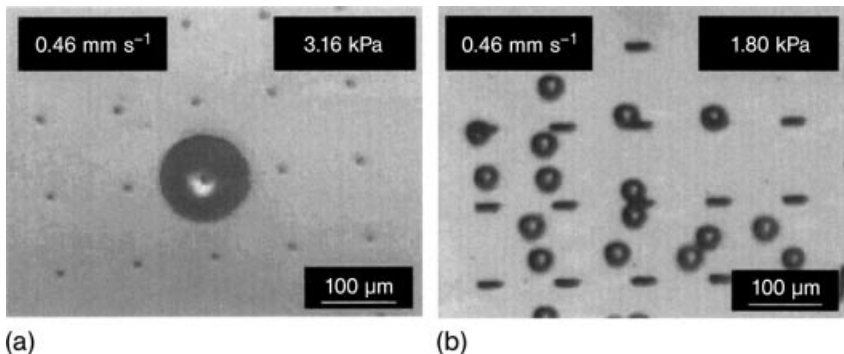
Figure 8.26 Droplet generation in device with (a) circular and (b) oblong microslots. From [155].

yielded monodispersed droplets (within 2%), whereas polydisperse droplets were obtained for the circular channels. The shape of the opening affected the droplet formation mechanism. Oblong openings with aspect ratio >3 facilitated the formation of a neck inside the channel and its eventual break-up, resulting in small and uniform droplets [156, 157].

8.2.3
Overlapping Microchannel and Micromesh Contactors

The overlapping microchannel and micromesh contactors described in Section 8.1.4 can also be utilized for contacting two immiscible liquid phases having lateral contact without mixing [81, 82, 158, 159]. In addition, other strategies have been employed. These include channels containing continuous or discontinuous ridges, selective patterning of channel walls with hydrophobic coatings and interfacial tension and flow rate control. The interfacial forces in liquid–liquid systems are often low and contact angles of the liquid–liquid/solid interface approach 90°. Thus, according to the Young–Laplace equation, the pressure difference that the interface can cope with is smaller.

Microchannels with continuous ridges (Figure 8.27) can be fabricated using a specially designed photomask pattern and careful control of etch time [160]. For the structure in Figure 8.27, the mask design had three separate channels, which, when isotropic etching in glass was allowed to proceed for a few minutes, became one
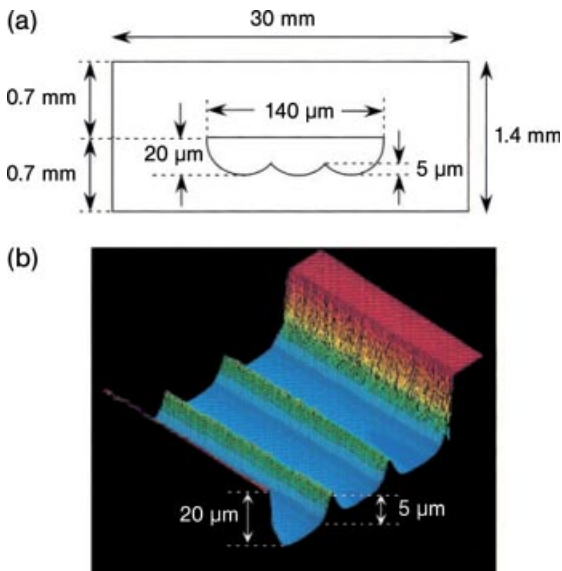
Figure 8.27 Microchannel contactor with guiding ridges. (a) Schematic cross-sectional view and (b) 3D image of the guide structures. From [160].

microchannel with guide structures at the bottom. In a slightly different design the ridges extend to the top wall and are intermittent [161]. Curved liquid–liquid interfaces form at the openings, stabilizing the liquid–liquid interface and allowing phase separation at the end-junction of the microchannel. The principle behind the continuous and intermittent ridge contactors is similar to the mesh and overlapping channel contactors; constricted opening(s) are formed between the two fluid streams which help to pin the interface. Such pinned interfaces between immiscible fluids can also be created by selective surface patterning of microchannels to create hydrophobic and hydrophilic paths. Water molecules would adhere to the hydrophilic channel surface with surface tension preventing the liquid from invading the hydrophobic region. Aqueous solutions introduced to the patterned microchannel will thus be confined to the hydrophilic region (Figure 8.28), provided that the pressure difference across the interface does not exceed the value imposed by the Young–Laplace equation [7]. Gravity does not affect the shape and geometry of the interface, provided that $Bo \ll 1$. For a fluid-liquid system with low interfacial tension and large density difference, $\gamma = 0.001 \, \text{N m}^{-1}$ and $\Delta\rho = 5000 \, \text{kg m}^{-3}$, in pores with diameters smaller than $d = 90 \, \mu\text{m}$, $Bo < 0.1$ and the interface shape is very close to spherical. For fluid pairs with larger interfacial tension or smaller density difference, even larger pores would give spherical menisci. In such cases, immiscible fluids can flow side by side along vertical interfaces or even on top of each other, defying gravity. The hydrophobic regions in Figure 8.28 were formed by multistream laminar flow. Hexadecane and a solution of an organotrichlorosilane (e.g. octadecyltrichlorosilane) in hexadecane were pumped into the preformed microchannels and were maintained under laminar flow for a predetermined period of time until self-assembled monolayers (SAMs) with full coverage formed. The areas where the silane solution passed were modified and became hydrophobic, whereas other areas remained hydrophilic [162]. Alternatively, the wetting properties of the surface can be selectively altered by photolithography using photocleavable SAMs [163] or graft polymerization [164].

Without stabilizing structures or surface patterning in lateral flow of immiscible fluids, there is a tendency for interfacial energy minimization to cause the streams to break up, in some cases converting to slug flow or more irregular forms. However, stratified flow without channel modification or stabilizing structure can be achieved by increasing Ca, i.e. using relatively low interfacial tension fluids, flow
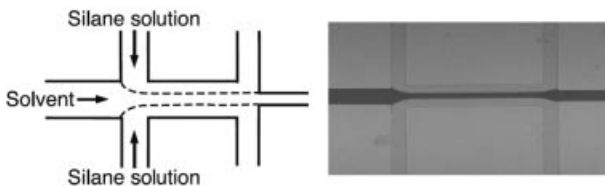
Figure 8.28 Schematic illustration of multistream laminar flows for selective patterning of channel walls and the corresponding image of aqueous flow inside channels after surface patterning. From [162].

rates sufficiently high to provide body forces counteracting the interfacial tension effects and fluids with sufficient viscosity difference [107, 165]. Stabilization of stratified flow can be aided by introducing surfactants which decrease the interfacial tension [166]. Such approaches can result in stratified flow and have the attraction of compatibility with simple channels, but are limited by the liquid pairs that can be used and contact times.

List of Symbols

a, b	constants of order 1
d	characteristic dimension
d_t	tube diameter
d_b	bubble diameter
d_d	droplet diameter
$d_{in,d}$	inlet diameter of dispersed phase channel
d_{or}	orifice diameter
D	diffusion coefficient
f	friction factor, Equation (8.4)
g	gravitational acceleration
L	length
P	pressure
Q	flow rate
R	pore radius
U	velocity
w	microchannel width
γ	interfacial tension
δ	film thickness
ε	volume fraction
ΔP	pressure difference between phases or pressure drop
$\Delta\rho$	density difference between phases
ε_0	$L_{droplet}/\pi w$
θ	contact angle or inclination angle from the horizontal
μ	viscosity
ν	kinematic viscosity
ν'	$\nu \times 1.6 \times 10^6$
ρ	density
Ω_{or}	orifice volume

Subscripts

b	bubble
c	continuous
d	dispersed
g	gas

in	inlet
l	liquid
m	mixture
or	orifice
s	slug

References

1 V. Hessel, P. Angeli, A. Gavriilidis, H. Lowe, Gas–liquid and gas–liquid–solid microstructured reactors: contacting principles and applications, *Ind. Eng. Chem. Res.*, **2005**, *44*, 9750–9769.

2 A. Günther, K.F. Jensen, Multiphase microfluidics: from flow characteristics to chemical and materials synthesis, *Lab Chip*, **2006**, *6*, 1487–1503.

3 C. Charcosset, H. Fessi, Membrane emulsification and microchannel emulsification processes, *Rev. Chem. Eng.*, **2005**, *21*, 1–32.

4 H. Song, D.L. Chen, R.F. Ismagilov, Reactions in droplets in microflulidic channels, *Angew. Chem. Int. Ed.*, **2006**, *45*, 7336–7356.

5 H. Mollet, A. Grubenmann, *Formulation Technology: Emulsions, Suspensions, Solid Forms*, Wiley-VCH Verlag GmbH, Weinheim, **2001**.

6 H.A. Stone, A.D. Stroock, A. Ajdari, Engineering flows in small devices: microfluidics toward a lab-on-a-chip, *Annu. Rev. Fluid Mech.*, **2004**, *36*, 381–411.

7 J. Atencia, D.J. Beebe, Controlled microfluidic interfaces, *Nature*, **2005**, *437*, 648–655.

8 V.S. Ajaev, G.M. Homsy, Modeling shapes and dynamics of confined bubbles, *Annu. Rev. Fluid Mech.*, **2006**, *38*, 277–307.

9 L.L. Shui, J.C.T. Eijkel, A. van den Berg, Multiphase flow in micro- and nanochannels, *Sens. Actuators B*, **2007**, *121*, 263–276.

10 B. Zhao, J.S. Moore, D.J. Beebe, Surface-directed liquid flow inside microchannels, *Science*, **2001**, *291*, 1023–1026.

11 J.W. Coleman, S. Garimella, Characterization of two-phase flow patterns in small diameter round and rectangular tubes, *Int. J. Heat Mass Transfer*, **1999**, *42*, 2869–2881.

12 T.S. Zhao, Q.C. Bi, Co-current air–water two-phase flow patterns in vertical triangular microchannels, *Int. J. Multiphase Flow*, **2001**, *27*, 765–782.

13 P. M–Y, Chung, M. Kawaji, The effect of channel diameter on adiabatic two-phase flow characteritics in micro-channels, *Int. J. Multiphase Flow*, **2004**, *30*, 735–761.

14 K.A. Triplett, S.M. Ghiaasiaan, S.I. Abdel-Khalik, D.L. Sadowski, Gas–liquid two-phase flow in microchannels. Part I: two-phase flow patterns, *Int. J. Multiphase Flow*, **1999**, *25*, 377–394.

15 A. Serizawa, Z. Feng, Z. Kawara, Two-phase flow in microchannels, *Exp. Thermal Fluid Sci.*, **2002**, *26*, 703–714.

16 C.-Y. Yang, C.-C. Shieh, Flow pattern of air–water and two-phase R-134a in small circular tubes, *Int. J. Multiphase Flow*, **2001**, *27*, 1163–1177.

17 S. Waelchli, P.R. von Rohr, Two-phase flow characteristics for gas–liquid microreactors, *Int. J. Multiphase Flow*, **2006**, *32*, 791–806.

18 M.K. Akbar, D.A. Akbar, S.M. Ghiaasiaan, On gas–liquid two-phase flow regimes in microchannels, *Int. J. Multiphase Flow*, **2003**, *29*, 855–865.

19 T. Cubaud, C.-M. Ho, Transport of bubbles in square microchannels, *Phys. Fluids*, **2004**, *16*, 4575–4585.

20 S. Irandoust, B. Andersson, Mass-transfer and liquid-phase reactions in a segmented 2-phase flow monolithic

catalyst reactor, *Chem. Eng. Sci.*, **1988**, *43*, 1983–1988.

21 G. Berčič, A. Pintar, The role of gas bubbles and liquid slug lengths on mass transport in the taylor flow through capillaries, *Chem. Eng. Sci.*, **1997**, *52*, 3709–3719.

22 T.C. Thulasidas, M.A. Abraham, R.L. Cerro, Dispersion during bubble train flow in capillaries, *Chem. Eng. Sci.*, **1999**, *54*, 61–76.

23 M.T. Kreutzer, F. Kapteijn, J.A. Moulijn, J.J. Heiszwolf, Multiphase monolith reactors: chemical reaction engineering of segmented flow in microchannels, *Chem. Eng. Sci.*, **2005**, *60*, 5895–5916.

24 T. Taha, Z.F. Cui, Hydrodynamics of slug flow inside capillaries, *Chem. Eng. Sci.*, **2004**, *59*, 1181–1190.

25 P. Garstecki, M.J. Fuerstman, H.A. Stone, G.M. Whitesides, Formation of droplets and bubbles in a microfluidic T-junction – scaling and mechanism of break-up, *Lab Chip*, **2006**, *6*, 437–446.

26 T. Cubaud, M. Tatineni, X.L. Zhong, C.M. Ho, Bubble dispenser in microfluidic devices, *Phys. Rev. E*, **2005**, *72*, 037302.

27 R. Xiong, M. Bai, J.N. Chung, Formation of bubbles in a simple co-flowing micro-channel, *J. Micromech. Microeng.*, **2007**, *17*, 1002–1011.

28 S. Laborie, C. Cabassud, L. Durand-Bourlier, J.M. Laine, Characterization of gas–liquid two-phase flow inside capillaries, *Chem. Eng. Sci.*, **1999**, *54*, 5723–5735.

29 H. Liu, C.O. Vandu, R. Krishna, Hydrodynamics of Taylor flow in vertical capillaries: flow regimes, bubble rise velocity, liquid slug length and pressure drop, *Ind. Eng. Chem. Res.*, **2005**, *44*, 4884–4897.

30 M.K. Akbar, S.M. Ghiaasiaan, Simulation of Taylor flow in capillaries based on the volume-of-fluid technique, *Ind. Eng. Chem. Res.*, **2006**, *45*, 5396–5403.

31 D. Qian, A. Lawal, Numerical study on gas and liquid slugs for Taylor flow in a T-junction microchannel, *Chem. Eng. Sci.*, **2006**, *61*, 7609–7625.

32 C. Amador, W. Salman, S. Sanguanpiyapan, A. Gavriilidis, P. Angeli, Effect of gas/liquid inlet conditions on slug length in taylor flow, in *Proceedings of the 5th International Conference of Multiphase Flow, Yokohama, 30 May–4 June*, **2004**, (CD-ROM).

33 G.I. Taylor, Deposition of a viscous fluid on the wall of a tube, *J. Fluid Mech.*, **1961**, *10*, 161–165.

34 T.C. Thulasidas, M.A. Abraham, R.L. Cerro, Bubble train flow in capillaries of circular and square cross-section, *Chem. Eng. Sci.*, **1995**, *50*, 183–199.

35 M.D. Giavedoni, F.A. Saita, The axisymmetric and plane case of a gas phase steadily displacing a Newtonian liquid – a simultaneous solution to the governing equations, *Phys. Fluids*, **1997**, *9*, 2420–2428.

36 W.B. Kolb, R.L. Cerro, The motion of long bubbles in tubes of square cross-section, *Phys. Fluids*, **1993**, *5*, 1549–1557.

37 F.P. Bretherton, The motion of long bubbles in tubes, *J. Fluid Mech.*, **1961**, *10*, 166–188.

38 J. Ratulowski, H.C. Chang, Marangoni effects of trace impurities on the motion of long gas bubbles in capillaries, *J. Fluid Mech.*, **1990**, *210*, 303–328.

39 P. Aussilous, D. Quéré, Quick deposition of a fluid on the wall of a tube, *Phys. Fluids*, **2000**, *12*, 2367–2371.

40 M.D. Giavedoni, F.A. Saita, The rear meniscus of a long bubble steadily displacing a Newtonian liquid in a capillary tube, *Phys.Fluids*, **1999**, *11*, 786–794.

41 R.K. Edvinsson, S. Irandoust, Finite element analysis of Taylor flow, *AIChE J.*, **1996**, *42*, 1815–1823.

42 M.T. Kreutzer, F. Kapteijn, J.A. Moulijn, C.R. Kleijn, J.J. Heiszwolf, Inertial and interfacial effects on pressure drop of Taylor flow in capillaries, *AIChE J.*, **2005**, *105*, 667–672.

43 A. Günther, S.A. Khan, M. Thalmann, F. Trachsel, K.F. Jensen, Transport and reaction in microscale segmented gas–liquid flow, *Lab Chip,* **2004,** *4,* 278–286.

44 W. Salman, A. Gavriilidis, P. Angeli, A model for predicting axial mixing during gas–liquid Taylor flow in microchannels at low Bodenstein numbers, *Chem. Eng. J.,* **2004,** *101,* 391–396.

45 H. Pedersen, C. Hovarth, Axial dispersion in a segmented gas–liquid flow, *Ind. Eng. Chem. Fundam.,* **1981,** *20,* 181–186.

46 M. Kreutzer, Hydrodynamics of Taylor flow in capillaries and monolith reactors, *PhD thesis,* Delft University, **2003.**

47 W. Salman, A. Gavriilidis, P. Angeli, Axial mass transfer in Taylor flow through circular microchannels, *AIChE J.,* **2007,** *53,* 1413–1428.

48 W. Salman, P. Angeli, A. Gavriilidis, Sample pulse broadening in Taylor flow microchannels for screening applications, *Chem. Eng. Techn.,* **2005,** *28,* 509–514.

49 S. Irandoust, S. Ertle, B. Andersson, Gas–liquid mass transfer in Taylor flow through a capillary, *Can. J. Chem. Eng.,* **1992,** *70,* 115–119.

50 C.O. Vandu, H. Liu, R. Krishna, Mass transfer from Taylor bubbles rising in single capillaries, *Chem. Eng. Sci.,* **2005,** *60,* 6430–6437.

51 J.M. van Baten, R. Krishna, CFD simulations of wall mass transfer for Taylor flow in circular capillaries, *Chem. Eng. Sci.,* **2005,** *60,* 1117–1126.

52 V. Haverkamp, Charakterisierung einer Mikroblasensäule zur Durchführung stofftransportlimitierter und/oder hochexothermer Gas/Flüssig-Reaktionen. *Dissertation,* Universität Erlangen-Nürnberg, Erlangen, (in Fortschritt-Bericht VDI, Reihe 3, Nr. 771), **2002.**

53 C.-C. Hsieh, S.-C. Yao, Development of a microscale passive gas–liquid separation system, in, *Proceedings of the 5th International Conference on Multiphase Flow, Yokohama,* 30 May–4 June, **2004,** paper No 566.

54 V. Hessel, W. Ehrfeld, T. Herweck, V. Haverkamp, H. Lüwe, J. Schiewe, C. Wille, T. Kern, N. Lutz, Gas–liquid microreactors: hydrodynamics and mass transfer, In *IMRET 4, Proceedings of the 4th International Conference on Microreaction Technology, Atlanta, GA,* March 5–9 2000, AIChE, New York, **2000,** pp. 174–186.

55 N. de Mas, A. Günther, M.A. Schmidt, K.F. Jensen, Microfabricated multiphase reactors for the selective direct fluorination of aromatics, *Ind. Eng. Chem. Res.,* **2003,** *42,* 698–710.

56 M.W. Losey, R.J. Jackman, S.L. Firebaugh, M.A. Schmidt, K.F. Jensen, Design and fabrication of microfluidic devices for multiphase mixing reaction, *J. Microelectromech. Syst.,* **2002,** *11,* 709–717.

57 M.W. Losey, M.A. Schmidt, K.F. Jensen, Microfabricated multiphase packed-bed reactors: characterization of mass transfer and reactions, *Ind. Eng. Chem. Res.,* **2001,** *40,* 2555–2562.

58 P.A. Ramachandran, R.V. Chaudhari, *Three-Phase Catalytic Reactors,* Gordon and Breach, New York, **1983.**

59 T. Inoue, M.A. Schmidt, K.F. Jensen, Microfabricated multiphase reactors for the direct synthesis of hydrogen peroxide from hydrogen and oxygen, *Ind. Eng. Chem. Res.,* **2007,** *46,* 1153–1160.

60 Y. Wada, M.A. Schmidt, K.F. Jensen, Flow distribution and ozonolysis in gas–liquid multichannel microreactors, *Ind. Eng. Chem. Res.,* **2006,** *45,* 8036–8042.

61 M.H. Al-Dahhan, F. Larachi, M.P. Dudukovic, A. Laurent, High-pressure trickle-bed reactors: a review, *Ind. Eng. Chem. Res.,* **1997,** *36,* 3292–3314.

62 D. Weaire, S. Hutzler, *Introduction to the Physics of Foams,* Clarendon Press, Oxford, **1999.**

63 G.N. Doku, W. Verboom, D.N. Reinhoudt, A. van den Berg, Microbubble beam (MBB), a potential dispersion mechanism for multiphase gas–liquid

microreactor systems, *Ind. Eng. Chem. Res.*, **2003**, *42*, 3721–3730.

64 A.M. Ganan-Calvo, J.M. Gordillo, Perfectly monodisperse microbubbling by capillary flow focusing, *Phys. Rev. Lett.*, **2001**, *87*, 274501.

65 A.M. Ganan-Calvo, M.A. Herrada, P. Garstecki, Bubbling in unbounded coflowing liquids, *Phys. Rev. Lett.*, **2006**, *96*, 124504.

66 A.M. Ganan-Calvo, Perfectly monodisperse microbubbling by capillary flow focusing: an alternate physical description and universal scaling, *Phys. Rev. Lett*, **2004**, *69*, 027301.

67 J.M. Gordillo, Z.D. Cheng, A.M. Ganan-Calvo, M. Marquez, D.A. Weitz, A new device for the generation of microbubbles, *Phys. Fluids*, **2004**, *16*, 2828–2834.

68 P. Garstecki, I. Gitlin, W. DiLuzio, G.M. Whitesides, E. Kumacheva, H.A. Stone, Formation of monodisperse bubbles in a microfluidic flow-focusing device, *Appl. Phys. Lett.*, **2004**, *85*, 2649–2651.

69 G.M. Whitesides, The origins and the future of microfluidics, *Nature*, **2006**, *442*, 368–373.

70 P. Garstecki, H.A. Stone, G.M. Whitesides, Mechanism for flow-rate controlled breakup in confined geometries: a route to monodisperse emulsions, *Phys. Rev. Lett.*, **2005**, *94*, 164501.

71 J.P. Raven, P. Marmottant, F. Graner, Dry microfoams: formation and flow in a confined channel, *Eur. Phys. J. B*, **2006**, *51*, 137–143.

72 M.W. Weber, R. Shandas, Computational fluid dynamics analysis of microbubble formation in microfluidic flow-focusing devices, *Microfluidics Nanofluidics*, **2007**, *3*, 195–206.

73 P. Garstecki, M.J. Fuerstman, G.M. Whitesides, Nonlinear dynamics of a flow-focusing bubble generator: an inverted dripping faucet, *Phys. Rev. Lett.*, **2005**, *94*, 234502.

74 E. Lorenceau, Y.Y.C. Sang, R. Hohler, S. Cohen-Addad, A high rate flow-focusing foam generator, *Phys. Fluids*, **2006**, *18*, 097103.

75 J.P. Raven, P. Marmottant, Periodic microfluidic bubbling oscillator: insight into the stability of two-phase microflows, *Phys. Rev. Lett.*, **2006**, *97*, 154501.

76 M.J. Jensen, H.A. Stone, H. Bruus, A numerical study of two-phase Stokes flow in an axisymmetric flow-focusing device, *Phys. Fluids*, **2006**, *18*, 077103.

77 P. Garstecki, G.M. Whitesides, Flowing crystals: Nonequilibrium structure of foam, *Phys. Rev. Lett.*, **2006**, *97*, 024503.

78 P. Lob, H. Pennemann, V. Hessel, g/l-Dispersion in interdigital micromixers with different mixing chamber geometries, *Chem. Eng. J.*, **2004**, *101*, 75–85.

79 M. Yasuno, S. Sugiura, S. Iwamoto, M. Nakajima, A. Shono, Monodispersed microbubble formation using microchannel technique, *AIChE J.*, **2004**, *50*, 3227–3233.

80 H. Pennemann, V. Hessel, H.J. Kost, H. Lowe, C. de Bellefon, Investigations on pulse broadening for catalyst screening in gas–liquid systems, *AIChE J.*, **2004**, *50*, 1814–1823.

81 J. Shaw, R. Nudd, B. Naik, *et al.*, Liquid–liquid extraction systems using micro-contactor arrays, in *Proceeedings of the 4th lnternational Conference on Miniaturized Chemical and Biochemical Analysis Systems, MicroTAS 2000*, **2000**, pp. 371–374.

82 D.A. Wenn, J.E.A. Shaw, B. Mackenzie, A mesh microcontactor for 2-phase reactions, *Lab Chip*, **2003**, *3*, 180–186.

83 J. Shaw, C. Turner, B. Miller, *et al.*, Reaction and transport coupling for liquid and liquid/gas microreactor systems, in *Proceedings of the 2nd International Conference on Microreaction Technology*, **1998**, pp. 176–180.

84 C. Turner, J. Shaw, B. Miller, *et al.*, Vapour stripping using a microcontactor, in *Proceeedings of the 4th lnternational*

Conference on Microreaction Technology, **2000**, pp. 106–113.

85 A. Hibara, S. Iwayama, S. Matsuoka, M. Ueno, Y. Kikutani, M. Tokeshi, T. Kitamori, Surface modification method of microchannels for gas–liquid two-phase flow in microchips, *Anal. Chem.*, **2005**, *77*, 943–947.

86 W.E. TeGrotenhuis, R.J. Cameron, V.V. Viswanathan,*et al.*, Solvent extraction and gas absorption using microchannel contactors, in *Proceedings of the 3rd International Conference on Microreaction Technology,* **1999**, pp. 541–549.

87 R. Abdallah, P. Magnico, B. Fumey, C. de Bellefon, CFD and kinetic methods for mass transfer determination in a mesh microreactor, *AIChE J.*, **2006**, *52*, 2230–2237.

88 C. Amador, P. Angeli, A. Gavriilidis,*et al.*, Meniscus shape, position and stability in straight pores, in *Proceedings of Annual AIChE Meeting*, **2003**, paper No. 277a.

89 G. Karimi, M. Kawaji, An experimental study of freely falling films in a vertical tube, *Chem. Eng. Sci.*, **1998**, *53*, 3501–3512.

90 A. Oron, S.H. Davis, S.G. Bankoff, Long-scale evolution of thin liquid films, *Rev. Mod. Phys.*, **1997**, *69*, 931–980.

91 V. Hessel, W. Ehrfeld, T. Herweck, V. Haverkamp, H. Löwe, J. Schiewe, C. Wille, T. Kern, N. Lutz, Gas–liquid micro reactors: hydrodynamics and mass transfer, in *Proceedings of the 4th International Conference on Microreaction Technology,* **2000**, pp. 174–186.

92 K.K. Yeong, A. Gavriilidis, R. Zapf, V. Hessel, Catalyst preparation and deactivation issues for nitrobenzene hydrogenation in a microstructured falling film reactor, *Catal. Today*, **2003**, *81*, 641–651.

93 K.K. Yeong, A. Gavriilidis, R. Zapf, H.-J. Kost, V. Hessel, A. Boyde, Characterization of liquid film in a

microstructured falling film reactor using laser scanning confocal microscopy, *Exp. Therm. Fluid Sci.*, **2006**, *30*, 463–472.

94 S.-Y. Lee, Y.P. Tsui, Succeed at gas–liquid contacting, *Chem. Eng. Prog.*, **1999**, July, 23–49.

95 S. Hardt, F. Doffing, H. Pennemann, Simulation of hydrodynamic dispersion in gas–liquid micro reactors, in *Proceedings of the 5th International Conference on Modeling and Simulation,* **2002**, pp. 54–57.

96 K.K. Yeong, A. Gavriilidis, R. Zapf, V. Hessel, Experimental studies of nitrobenzene hydrogenation in a microstructured falling film reactor, *Chem. Eng. Sci.*, **2004**, *59*, 3491–3494.

97 C. de Bellefon, T. Lamouille, N. Pestre, F. Bornette, H. Pennemann, F. Neumann, V. Hessel, Asymmetric catalytic hydrogenations at micro-litre scale in a helicoidal single channel falling film micro-reactor, *Catal. Today*, **2005**, *110*, 179–187.

98 B.K. Vankayala, P. Lob, V. Hessel, G. Menges, C. Hofmann, D. Metzke, H.J. Kost, U. Krtschil, Scale-up of process intensifying falling film microreactors to pilot production scale, in *Proceedings of the 1st International Congress on Green Process Engineering,* Toulouse, France, 24–26 April **2007**.

99 J.M. Commenge, T. Obein, G. Genin, X. Framboisier, S. Rode, V. Schanen, R. Pitiot, M. Matlosz, Gas-phase residence time distribution in a falling-film microreactor, *Chem. Eng. Sci.*, **2006**, *61*, 597–604.

100 R. Dreyfus, P. Tabeling, H. Willaime, Ordered and disordered patterns in two-phase flows in microchannels, *Phys. Rev. Lett.*, **2003**, *90*, 144505.

101 J.H. Xu, G.S. Luo, S.W. Li, G.G. Chen, Shear force induced monodisperse droplet formation in a microfluidic device by controlling wetting properties, *Lab Chip*, **2006**, *6*, 131–136.

102 P. Guillot, A. Colin, Stability of parallel flows in a microchannel after

a T junction, *Phys. Rev. E*, **2005**, *72*, 066301.

103 T. Thorsen, R.W. Roberts, F.H. Arnold, S.R. Quake, Dynamic pattern formation in a vesicle-generating microfluidic device, *Phys. Rev. Lett.*, **2001**, *86*, 4163–4166.

104 J.D. Tice, H. Song, A.D. Lyon, R.F. Ismagilov, Formation of droplets and mixing in multiphase microfluidics at low values of the Reynolds and the capillary numbers, *Langmuir*, **2003**, *19*, 9127–9133.

105 B.J. Adzima, S.S. Velankar, Pressure drops for droplet flows in microfluidic channels, *J. Micromech. Microeng.*, **2006**, *16*, 1504–1510.

106 J.R. Burns, C. Ramshaw, The intensification of rapid reactions in multiphase systems using slug flow in capillaries, *Lab Chip*, **2001**, *1*, 10–15.

107 B. Zheng, J.D. Tice, R.F. Ismagilov, Formation of droplets of alternating composition in microfluidic channels and applications to indexing of concentrations in droplet-based assays, *Anal. Chem.*, **2004**, *76*, 4977–4982.

108 M.N. Kashid, I. Gerlach, S. Goetz, J. Franzke, J.F. Acker, F. Platte, D.W. Agar, S. Turek, Internal circulation within the liquid slugs of a liquid–liquid slug-flow capillary microreactor, *Ind. Eng. Chem. Res.*, **2005**, *44*, 5003–5010.

109 K. Handique, M.A. Burns, Mathematical modeling of drop mixing in a slit-type microchannel, *J. Micromech. Microeng.*, **2001**, *11*, 548–554.

110 G. Dummann, U. Quittmann, L. Gröschel, D.W. Agar, O. Wörz, K. Morgenschweis, The capillary-microreactor: a new reactor concept for the intensification of heat and mass transfer in liquid–liquid reactions, *Catal. Today*, **2003**, *79–80*, 433–439.

111 H. Song, D.L. Chen, R.F. Ismagilov, Reactions in droplets in microflulidic channels, *Angew. Chem. Int. Ed.*, **2006**, *45*, 7336–7356.

112 F. Sarrazin, K. Loubière, L. Prat, C. Gourdon, T. Bonometti, J. Magnaudet, Experimental and numerical study of droplets hydrodynamics in microchannels, *AIChE J.*, **2006**, *52*, 4061–4070.

113 H. Song, M.R. Bringer, J.D. Tice, C.J. Gerdts, R.F. Ismagilov, Experimental test of scaling of mixing by chaotic advection in droplets moving through microfluidic channels, *Appl. Phys. Lett.*, **2003**, *83*, 4664–4666.

114 J.H. Xu, S.W. Li, J. Tan, Y.J. Wang, G.S. Luo, Controllable preparation of monodisperse O/W and W/O emulsions in the same microfluidic device, *Langmuir*, **2006**, *22*, 7943–7946.

115 T. Nisisako, T. Torii, T. Higuchi, Droplet formation in a microchannel network, *Lab Chip*, **2002**, *2*, 24–26.

116 J.M. Rallison, The deformation of small viscous drops and bubbles in shear flows, *Annu. Rev. Fluid Mech.*, **1984**, *16*, 45–66.

117 H.A. Stone, Dynamics of drop deformation and breakup in viscous fluids, *Annu. Rev. Fluid Mech.*, **1994**, *26*, 65–102.

118 V. Cristini, Y.C. Tan, Theory and numerical simulation of droplet dynamics in complex flows – a review, *Lab Chip*, **2004**, *4*, 257–264.

119 J.H. Xu, S.W. Li, J. Tan, Y.J.Wang, G.S. Luo, Preparation of highly monodisperse droplet in a T-junction microfluidic device, *AIChE J.*, **2006**, *52*, 3005–3010.

120 Y.C. Tan, V. Cristini, A.P. Lee, Monodispersed microfluidic droplet generation by shear focusing microfluidic device, *Sens. Actuators B*, **2006**, *114*, 350–356.

121 J.H. Xu, G.S. Luo, G.G. Chen, Y.J. Wang, Experimental and theoretical approaches on droplet formation from a micrometer screen hole, *J. Membr. Sci.*, **2005**, *266*, 121–131.

122 S. van der Graaf, C.G.P.H. Schroen, R.G.M. van der Sman, R.M. Boom, Influence of dynamic interfacial tension on droplet formation during membrane

emulsification, *J. Colloid Interface Sci.*, **2004**, *277*, 456–463.

123 C. Cramer, P. Fischer, E.J. Windhab, Drop formation in a co-flowing ambient fluid, *Chem. Eng. Sci.*, **2004**, *59*, 3045–3058.

124 A.M. Ganan-Calvo, P. Riesco-Chueca, Jetting–dripping transition of a liquid jet in a lower viscosity co-flowing immiscible liquid: the minimum flow rate in flow focusing, *J. Fluid Mech.*, **2006**, *553*, 75–84.

125 P.B. Umbanhowar, V. Prasad, D.A. Weitz, Monodisperse emulsion generation via drop break off in a coflowing stream, *Langmuir*, **2000**, *16*, 347–351.

126 S.L. Anna, N. Bontoux, H.A. Stone, Formation of dispersions using flow focusing in microchannels, *Appl. Phys. Lett.*, **2003**, *82*, 364–366.

127 S.L. Anna, H.C. Mayer, Microscale tipstreaming in a microfluidic flow focusing device, *Phys. Fluids*, **2006**, *18*, 121512.

128 T. Ward, M. Faivre, M. Abkarian, H.A. Stone, Microfluidic flow focusing: drop size and scaling in pressure versus flow-rate-driven pumping, *Electrophoresis*, **2005**, *26*, 3716–3724.

129 Q.Y. Xu, M. Nakajima, The generation of highly monodisperse droplets through the breakup of hydrodynamically focused microthread in a microfluidic device, *Appl. Phys. Lett.*, **2004**, *85*, 3726–3728.

130 S. Takeuchi, P. Garstecki, D.B. Weibel, G.M. Whitesides, An axisymmetric flow-focusing microfluidic device, *Adv. Mater.*, **2005**, *17*, 1067–1072.

131 L. Yobas, S. Martens, W.L. Ong, N. Ranganathan, High-performance flow-focusing geometry for spontaneous generation of monodispersed droplets, *Lab Chip*, **2006**, *6*, 1073–1079.

132 Z.H. Nie, S.Q. Xu, M. Seo, P.C. Lewis, E. Kumacheva, Polymer particles with various shapes and morphologies produced in continuous microfluidic reactors, *J. Am. Chem. Soc.*, **2005**, *127*, 8058–8063.

133 L. Martin-Banderas, A. Rodriguez-Gil, A. Cebolla, S. Chavez, T. Berdun-Alvarez, J.M.F. Garcia, M. Flores-Mosquera, A.M. Ganan-Calvo, Towards high-throughput production of uniformly encoded microparticles, *Adv. Mater.*, **2006**, *18*, 559–564.

134 D.J.E. Harvie, M.R. Davidson, J.J. Cooper-White, M. Rudman, A parametric study of droplet deformation through a microfluidic contraction: low viscosity Newtonian droplets, *Chem. Eng. Sci.*, **2006**, *61*, 5149–5158.

135 D.R. Link, S.L. Anna, D.A. Weitz, H.A. Stone, Geometrically mediated breakup of drops in microfluidic devices, *Phys. Rev. Lett.*, **2004**, *92*, 054503.

136 V. Sibillo, G. Pasquariello, M. Simeone, V. Cristini, S. Guido, Drop deformation in microconfined shear flow, *Phys. Rev. Lett.*, **2006**, *97*, 054502.

137 M. De Menech, Modeling of droplet breakup in a microfluidic T-shaped junction with a phase-field model, *Phys. Rev. E*, **2006**, *73*, 031505.

138 V. Haverkamp, W. Ehrfeld, K. Gebauer, V. Hessel, H. Lowe, T. Richter, C. Wille, The potential of micromixers for contacting of disperse liquid phases, *Fresenius' J. Anal. Chem.*, **1999**, *364*, 617–624.

139 H. Pennemann, S. Hardt, V. Hessel, P. Lob, F. Weise, Micromixer based liquid–liquid dispersion, *Chem. Eng Tech.*, **2005**, *28*, 501–508.

140 P. Lob, H. Pennemann, V. Hessel, Y. Men, Impact of fluid path geometry and operating parameters on l/l-dispersion in interdigital micromixers, *Chem. Eng. Sci.*, **2006**, *61*, 2959–2967.

141 S. Hardt, F. Jiang, F. Schonfeld, A computational analysis of the hydrodynamic instability of a liquid jet focused into a converging microchannel, *Int. J. Multiphase Flow*, **2005**, *31*, 739–756.

142 A.J. Gijsbertsen-Abrahamse, A. van der Padt, R.M. Boom, Status of cross-flow membrane emulsification and outlook for industrial application, *J. Membr. Sci.*, **2004**, *230*, 149–159.

143 J. de Jong, M.J. Geerken, R.G.H. Lammertink, M. Wessling, Porous microfluidic devices – fabrication and applications, *Chem. Eng. Tech.*, **2007**, *30*, 309–315.

144 S. Sugiura, M. Nakajima, J.H. Tong, H. Nabetani, M. Seki, Preparation of monodispersed solid lipid microspheres using a microchannel emulsification technique, *J. Colloid Interface Sci.*, **2000**, *227*, 95–103.

145 S. Sugiura, M. Nakajima, S. Iwamoto, M. Seki, Interfacial tension driven monodispersed droplet formation from microfabricated channel array, *Langmuir*, **2001**, *17*, 5562–5566.

146 S. Sugiura, M. Nakajima, M. Seki, Prediction of droplet diameter for microchannel emulsification, *Langmuir*, **2002**, *18*, 3854–3859.

147 S. Sugiura, M. Nakajima, M. Seki, Effect of channel structure on microchannel emulsification, *Langmuir*, **2002**, *18*, 5708–5712.

148 S. Sugiura, M. Nakajima, T. Oda, M. Satake, M. Seki, Effect of interfacial tension on the dynamic behavior of droplet formation during microchannel emulsification, *J. Colloid Interface Sci.*, **2004**, *269*, 178–185.

149 I. Kobayashi, K. Uemura, M. Nakajima, Formulation of monodisperse emulsions using submicron-channel arrays, *Colloids Surf. A*, **2007**, *296*, 285–289.

150 C. Priest, S. Herminghaus, R. Seemann, Generation of monodisperse gel emulsions in a microfluidic device, *Appl. Phys. Lett.*, **2006**, *88*, 024106.

151 E.M. Chan, A.P. Alivisatos, R.A. Mathies, High-temperature microfluidic synthesis of CdSe nanocrystals in nanoliter droplets, *J. Am. Chem. Soc.*, **2005**, *127*, 13854–13861.

152 A.J. Abrahamse, R. van Lierop, R.G.M. van der Sman, A. van der Padt, R.M. Boom, Analysis of droplet formation and interactions during cross-flow membrane emulsification, *J. Membr. Sci.*, **2002**, *204*, 125–137.

153 M.J. Geerken, R.G.H. Lammertink, M. Wessling, Tailoring surface properties for controlling droplet formation at microsieve membranes, *Colloids Surf. A*, **2007**, *292*, 224–235.

154 I. Kobayashi, S. Mukataka, M. Nakajima, Novel asymmetric through-hole array microfabricated on a silicon plate for formulating monodisperse emulsions, *Langmuir*, **2005**, *21*, 7629–7632.

155 I. Kobayashi, M. Nakajima, K. Chun, Y. Kikuchi, H. Fujita, Silicon array of elongated through-holes for monodisperse emulsion droplets, *AIChE J.*, **2002**, *48*, 1639–1644.

156 I. Kobayashi, S. Mukataka, M. Nakajima, CFD simulation and analysis of emulsion droplet formation from straight-through microchannels, *Langmuir*, **2004**, *20*, 9868–9877.

157 I. Kobayashi, S. Mukataka, M. Nakajima, Effect of slot aspect ratio on droplet formation from silicon straight-through microchannels, *J. Colloid Interface Sci.*, **2004**, *279*, 277–280.

158 C. Turner, J. Shaw, B. Miller, *et al.*, Solvent extraction using micro-mesh reactors, in *Proceedings of the 4th International Conference on Microreaction Technology*, **2000**, pp. 334–340.

159 W.E. TeGrotenhuis, R.J. Cameron, M.G. Butcher, *et al.*, Microchannel devices for efficient contacting of liquids in solvent extraction, in *Proceedings of the 2nd International Conference on Microreaction Technology*, **1998**, pp. 329–334.

160 M. Tokeshi, T. Minagawa, K. Uchiyama, *et al.*, Continuous-flow chemical processing on a microchip by combining microunit operations and a multiphase flow network, *Anal. Chem.*, **2002**, *74*, 1565–1571.

161 T. Maruyama, T. Kaji, T. Ohkawa, *et al.*, Intermittent partition walls promote solvent extraction of metal ions in a microfluidic device, *Analyst*, **2004**, *129*, 1008–1013.

162 B. Zhao, J.S. Moore, D.J. Beebe, Surface-directed liquid flow inside microchannels, *Science*, **2001**, *291*, 1023–1026.

163 B. Zhao, J.S. Moore, D.J. Beebe, Principles of surface-directed liquid flow in microfluidic channels, *Anal. Chem.*, **2002**, *74*, 4259–4268.

164 S.W. Hu, X.Q. Ren, M. Bachman, *et al.*, Surface-directed, graft polymerization within microfluidic channels, *Anal. Chem.*, **2004**, *76*, 1865–1870.

165 P. Kuban, J. Berg, P.K. Dasgupta, Vertically stratified flows in microchannels. Computational simulations and applications to solvent extraction and ion exchange, *Anal. Chem.*, **2003**, *75*, 3549–3556.

166 V. Reddy, J.D. Zahn, Interfacial stabilization of organic–aqueous two-phase microflows for a miniaturized DNA extraction module, *J. Colloid Interface Sci.*, **2005**, *286*, 158–165.